9-11-2015 12:00 AM

Structure-Function Relationship of the Brain: A comparison between the 2D Classical Ising model and the Generalized Ising model

Pubuditha M. Abeyasinghe
The University of Western Ontario

Supervisor
Dr. Andrea Soddu
The University of Western Ontario

Graduate Program in Physics

A thesis submitted in partial fulfillment of the requirements for the degree in Master of Science

STRUCTURE-FUNCTION RELATIONSHIP OF THE BRAIN: A COMPARISON BETWEEN THE 2D CLASSICAL ISING MODEL AND THE GENERALIZED ISING MODEL

(Thesis format: Monograph)

by

Pubuditha Abeyasinghe

Graduate Program in Physics

A thesis submitted in partial fulfillment

of the requirements for the degree of

Master of Science

The School of Graduate and Postdoctoral Studies

The University of Western Ontario

London, Ontario, Canada

Abstract

There is evidence that the functional patterns of the brain observed at rest using fMRI are sustained by a structural architecture of axonal fiber bundles. As neuroimaging techniques advance with time, the relationship between structure and function has become the object of many studies in neuroscience. As recently suggested, the well-defined connectivity structure found in the brain can be used to understand the self organization of the brain at rest, as well as to infer the functional connectivity patterns of the brain using different models. These models include the Kuramoto model, which studies synchronization, and the two-dimensional classical Ising model, which studies the global dynamics of the brain at the critical temperature. These models have been successful in capturing the underlying properties of the brain. To extend this understanding, our objective is to develop the generalized Ising model, following the lesson from the two-dimensional Ising model, as the generalized Ising model could be simulated using the anatomical structure of the brain. This model can then be used to study functional information integration and segregation in the brain at rest. Thus, the primary research question would be: can the generalized Ising model explain the functional behaviour of the resting brain at the critical temperature? Preliminary analyses were carried out to determine the critical temperature of the models and to compare the correlation distributions. Further analyses were carried out using graph theory considering the brain as a network. By observing the results obtained from our simulations, it can be inferred that there is a temperature that is different from the critical temperature of the model at which the generalized Ising model shows a match with the empirical functional connectivity. At that temperature, the generalized Ising model could be used to study the global dynamics, as well as the local dynamics of the brain.

Keywords: Ising model, Structure and function of the brain, Graph Theory

Dedication

To my family,

for their unconditional love and care...

To my adorable nephew,

for his priceless love and the biggest heart...

Acknowledgement

The preparation and compilation of this Dissertation would not have been possible if not for the assistance and support given to me by my seniors, family and friends.

I would like to take this opportunity to extend my gratitude to my advisor, Prof. Andrea Soddu for the assistance he rendered to me and for the amount of tolerance he demonstrated when directing me in the correct path to make this dissertation a success. I must state that it was a privilege to be guided by you. My extended gratitude goes towards my advisory committee for spending their time to evaluate my work and to have all the meaningful discussions in order to give me the opportunity to learn.

I also wish to extend my sincere thanks to Dr. Tushar K. Das for the support and for the motivation he provided for my success from the beginning. Further, I thank all the members in our group whom I met at some point in the past two years.

My heartfelt thanks are extended to all my friends who stood beside me during this journey and who were supportive throughout.

Further, I thank my two brothers and sister for always being there with me whenever I need, despite miles apart.

Finally, I thank my parents for being the biggest and the strongest pillers of my life. Even though they are thousands of miles away, they managed to be with me the entire journey. I would have performed less if it was not for their love and care. Special thanks goes to them, for understanding my flaws, accepting me for who I am and for being closer to my heart always.

Contents

List of Figures

List of Tables

Chapter 1

Introduction

1.1 Introduction

The human brain draws the attention of neuroscientists because of its complex and mysterious behaviour. It is one of the organs that scientists are still struggling to understand. The understanding available so far about the brain is mostly due to developments in brain imaging techniques. However, we are trying to build a bridge between mathematical modelling and the biological aspects of the human brain to open up new opportunities to widen our understanding of its behaviour.

That being said, the introduction of mathematics to biology and medicine has drawn much interest recently. Mathematical models are built in general to describe some aspects of nature in a numerical manner such that they could be used to predict unseen behaviours in nature. The spatial scale of modelling varies depending on the scale of the expected end result. In this research, as we are discussing the behaviour of the brain (which has a complex structure), it is not realistic to talk in terms of the nano-scale or micro-scale using the available resources. Thus rather than applying mathematical modelling for our studies at the finest scale, the models are being developed at macroscopic level.

However, our brain is comprised of neurons, which form different types of structural networks. This structural or the anatomical connectivity allows electrical signals to pass through and exchange information among different regions of the brain. On the other hand, the neurons create functional networks depending on their functionality, such as cognition and perception. Even though there are discussions about a possible connection between these two types of connectivity patterns (structural and functional), the exact connection is still debatable. Nevertheless, the purpose of this research is to develop a tool that enables us to find the relationship between the structure and the function of the brain using computational modelling. In terms of modelling, we use the structural connectivity obtained from brain imaging as an input for the simulations, and we will be comparing the output of the model with the empirical data of the functional activity in the brain to find the structure-function relationship.

1.2 Motivation & Objectives

As per the common understanding, inside the brain, there are billions of neurons that collectively are the foundation of who we are. This fact makes the brain more difficult to understand and still there is no experimental method, or an imaging technique, that can explain the complete behaviour of the brain at a single neuronal level. However, our objective was to find a mathematical model, that can be used to simplify our understanding at the macroscopic scale and can be advanced to better spatial resolution in the future. For this purpose, we introduce the generalized Ising model as a good candidate for our study.

The generalization was performed starting with the two-dimensional classical Ising model which explains the interactions of magnetic spins. The spins are arranged in a two-dimensional lattice which is in contact with a heat bath. The model has only one model parameter, the tem-

perature of the heat bath. Arrangements of spins change as a function of temperature and as a result of that, the properties of this system change. During the studies of this model, a temperature called the critical temperature was identified as the temperature which differentiate the configurations of spins into two categories, order and disorder. In previous work related to neuroscience and modelling, the two-dimensional classical Ising model has been studied at different temperatures and has been compared with the dynamics of the brain function, which resulted in providing a good match between the model and the empirical data at the critical temperature. Thus we use the two-dimensional classical Ising model and generalize it by introducing the structural connectivity of the brain for the simulations of the model.

Therefore, briefly, the problem we are investigating in this research is: can the generalized Ising model be used to explain the structure-function relationship of the brain at the critical temperature? If so, can this model be used to predict the functional changes in the brain in the presence of a brain disorder by using the observed structural changes? Initially we are carrying out this research on healthy subjects, and later on, we can expand our limits towards patients with brain disorders due to severe brain injuries in order to answer the second question.

1.3 Thesis Outline

This thesis contains five chapters organized as follows. The first chapter gives a general introduction. The second chapter will provide the necessary understanding of the background of the research. It will describe the basics of neuronal communication as well as the neuroimaging techniques. Furthermore, detailed descriptions of computational models that have been used will be given. The third chapter will explain the experimental methodology, including the computer simulations of the models. The results of the simulations are shown in the next chapter. Finally, the last chapter will contain the conclusions of the work followed by a discussion. This will include possible directions for future research.

Chapter 2

Background & related work

2.1 Overview

This chapter intends to provide the background of the research. At the beginning, we will explain the neuronal communication in the brain with a brief explanation of the nature of functional and structural connectivity. Then we will talk about two different brain imaging techniques, one of which is being used to study the behaviour of the brain, the functional Magnetic Resonance Imaging (fMRI), and the other of which is being used to study the structure of the brain, Diffusion Weighted Imaging (DWI). This discussion will be followed by an introduction to two computer-simulated models that have been used in the past in order to model the dynamics of the brain. The reason for choosing the Ising model out of the two models will be presented as well. After that, the generalized Ising model will be introduced as the model we propose to model the dynamics of the brain as well as to find the structure-function relationship in the brain. This will be followed by an introduction to the graph theory that we apply in order to compare the classical Ising model and the generalized Ising model in this context. This description will include an introduction to some important graph theoretical properties.

2.2 Neuronal Communication

The human brain is made up of billions of neurons, which are the foundation of all the thoughts, feelings and memories that constitute our sense of identity. The most important thing to maintaining a high efficiency while performing any task is *'communication'*, and it is maintained in our brains via neurons. They are used to communicate among different regions of the brain that are functionally specialized for different tasks. Thus, by integrating the work of separate regions, it is possible to coordinate different functions of different organs in the body.

Neurons are sensors that can pass information through electrochemical signals. They can generate electrical impulses in response to different types of signals they receive, and transmit those signals to other cells. In order to do this, a neuron is comprised of two basic parts: the cell body and the axon (Figure 2.1). The cell body contains several dendrites distributed much like the branches of a tree. This branching architecture of the dendrites allows the cell body to receive signals from a number of cells. The signals entering the neurons are received via the dendrites, and an action potential is generated according to the received signals. The action potential is generated due to the charged atoms (ions) in the cells.

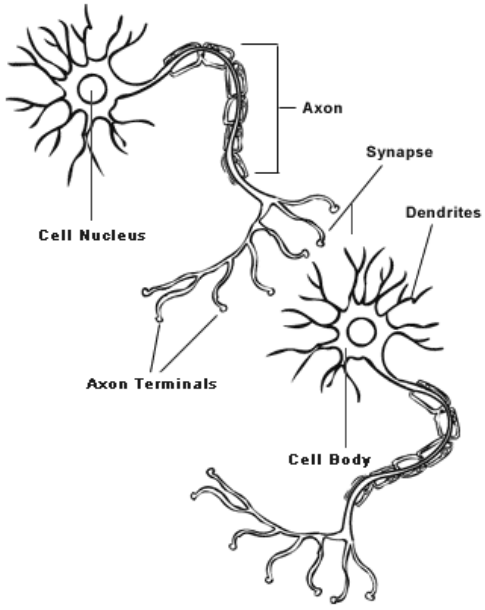

Figure 2.1: Main components of a neuron [1]

A cell is made out of chambers that contain various types of ions. Depending on the incoming signals, these chambers release different amounts of ions in different types. Due to this, a voltage difference is created which gives rise to a small current. Therefore, when the neuronal impulse begins, the potential of the cell changes dramatically. This change is called the action potential. The action potentials are transmitted to the axon terminals through relatively long axons. At the end of the neuron (i.e. axon terminal), a chemical messenger called a *neurotransmitter* is then released to the synapses, which is the junction between two nerve cells (Figure 2.1). This neurotransmitter binds with the receptors at the dendrites of the next cell. The receptors act as the source of the action potential of that cell. This process is repeated billions of times, and the electrical impulses are transmitted throughout.

However, it is a well-known fact that the neurons do not function as individual units. Instead, hundreds of neurons, which are synchronized together, collectively form a patch of cortex. Apparently, inside the brain there exist large groups of such patches of cortices, which can either be synchronized or desynchronized abruptly, creating various sizes of temporary

systems based on the behaviour of the brain. The functional connectivity, which does not carry information related to the directionality of the information transfer, could be used to describe the interactions between these patches of cortices. Neurons pass signals very fast (i.e even with a speed greater than $100ms^{-1}$ sometimes) compared to the time window chosen in imaging (which varies from $0.3s - 4s$ depending on the type of the image). Therefore, even though there is a directionality in the interactions of the patches of cortices, the functional connectivity can be used because we are studying the interactions in a time window over which the effects of directionality might be washed away. Thus a brief explanation about the functional connectivity will be provided in the next section, followed by an explanation about the anatomical (structural) connectivity.

2.2.1 Functional Connectivity

Functional connectivity in the brain is a concept that is still up for debate in neuroscience related research. However, the most popular definition used especially in fMRI is that functional connectivity in the brain is the correlation between spatially separated neurophysiological units or in other words patches of cortices [4]. The measured temporal correlation of the activity of these patches of cortices is considered to be the signature of functional connectivity. These correlations emerge from the task-specific patches of cortices, which have emergent properties that individual neurons do not have [5].

That being said, functional Magnetic Resonance Imaging (fMRI) is a good tool discussed so far that could be used to understand the insights of functional connectivity. In fMRI, a Blood Oxygen Level Dependent (BOLD) signal is recorded from a volumetric pixel (voxel) with an average size of 55 mm^3. Following the statistics, this voxel contains 5.5 million neurons and $2 - 5 \times 10^{10}$ synapses [6]. Thus, the BOLD time variation observed for a single voxel in fMRI results due to a population of neurons, instead of a single neuron. Then, the emerging question is, *will this spatial resolution be enough to understand the functional connectivity of*

the brain? The answer depends on the scale of the problem that we are looking at. If we want to understand the functional connectivity in the scale of a patch of cortex, instead of the single neuronal level, the given fMRI spatial resolution could be used. Using that, the mean activity of a group of neurons can be captured. This could be relevant to understand phenomena like consciousness, which also emerges from a collective behaviour of neurons.

2.2.2 Structural Connectivity

Structural connectivity provides details about the connections the neurons or the patch of cortices in the brain hold. In other words, it gives the structure of the neuronal connections. The interconnectivity pattern of the brain at the neuronal level is one of the most complex environments. Its complexity varies from the single neuronal level to the connections of brain regional levels through different models of connectivity. Studying structural connectivity at the neuronal level or micro-scale, has not been feasible due to its complexity. It might not be necessary either, as there is an enormous degree of confirmation for the fact that the cognitive functions of humans depend on the collective activity of large populations of neurons, instead of individual neurons [7]. In addition to this, it is known there are momentary plastic changes in neuronal levels including structural remodelling [8, 9]. There is much variability associated with the connections at the micro-scale and these variabilities could be multiplied by orders of billions as there are as many neurons in the brain. Thus, we focus on structural connectivity in more technically feasible, as well as meaningful, level of scale. In fact, there are wide ranges of experimental techniques at the macro-scale that could be used to study the pathways among brain regions. One of the techniques is Diffusion Tensor Imaging (DTI), which we used for this research and will be discussed further in this context. As a brief note, DTI captures the tracks of white matter in the brain using the diffusion of water molecules. However, structural connectivity is a critical determinant of the dynamics of the brain. In contrast, the functional behaviour of the brain has the ability to redesign the anatomical structure during developmental stages [10].

2.3 Brain Imaging

Brain imaging is an important portion of research in several fields, including biology, physics and psychology. There are lot of ongoing research for the development of different brain imaging techniques. Some of them include Magnetic Resonance Imaging (MRI), functional Magnetic Resonance Imaging (fMRI), Diffusion Tensor Imaging (DTI) and Positron Emission Tomography (PET). We are interested in fMRI and DTI because we are investigating the relationship between the structure and the function of the brain. Therefore, fMRI and DTI techniques will be discussed further.

2.3.1 Functional Magnetic Resonance Imaging (fMRI)

Functional Magnetic Resonance Imaging (fMRI), is an MRI technique that is being used to measure the functional behaviour of the brain by measuring the BOLD signal. Since the discovery of fMRI in the 1990s, it has been a very popular method for brain imaging for several reasons. One reason is that it does not require the injection of radioactive substances into the brain as in PET. Another reason is that the fMRI technique has better spatial resolution than PET [11]. However, there are basic hardware requirements in MRI devices. First and foremost, it should have a magnet capable of having high magnetic field strengths. This magnet acquire its strength by an external power supply. Next, it should contain a gradient coil that can produce a field gradient. The gradient coil produces a secondary magnetic field when the current passes through it, which will distort the main magnetic field. This allows the spatial identification of the MR signal. Furthermore, there should be a radio frequency coil that can transmit and receive radio frequency oscillations, and a computer to acquire signals and compose the MR images [12]. A schematic diagram of these components in an MRI device is shown in Figure 2.2.

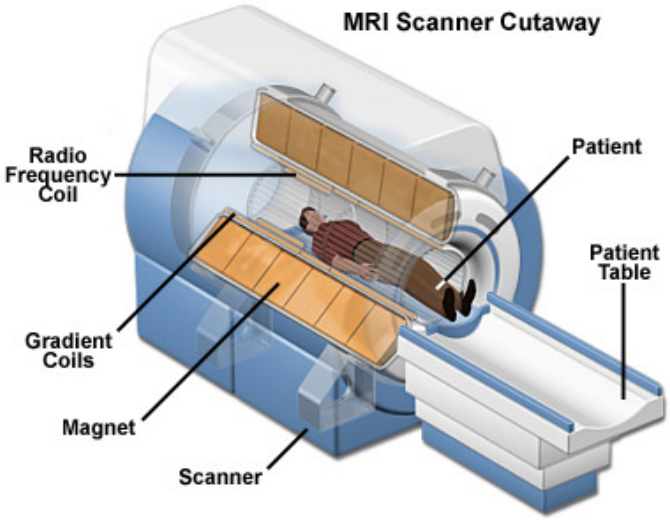

Figure 2.2: Main components of an MRI system. Image courtesy of the National Magnetic Field Laboratory [2]

The MRI signal is generated from the highly abundant protons in brain tissues in the form of water or fat. Depending on the amount of protons in the tissue, the strength of the MR signal varies. In the absence of a magnetic field, the magnetic moments of these protons are randomly oriented. When a strong magnetic field is applied, they interact with the applied field and partially align with the field behaving like tiny bar magnets. Due to this alignment, a small amount of magnetization is created. Then using a radio frequency signal, a perturbation is introduced to these protons and when it is removed, the protons will take some time (relaxation time) to reposition. In the meantime, the observed magnetization will vary and it will gives rise to a detectable signal in the MRI device. If the relaxation time is long, then the MR signal will be strong and it will be weak otherwise.

The MRI technique was extended to fMRI in order to obtain information about the biological functions of the brain in the 1990s [13]. The basic principle of the fMRI is defined as the detection of changes in the level of oxygen in the blood. This is called the BOLD effect. When

there is neuronal activation in the brain, the blood flow into that activated area increases as demanded by neurons to supply energy [14]. The energy needed is provided by supplying more oxygenated blood. Thus, when a set of neurons activates, more oxyhaemoglobin (which is diamagnetic) is delivered than deoxyhaemoglobin (which is paramagnetic). Oxyhaemoglobin can be magnetized by applying an external magnetic field, in the same direction as the external field (diamagnetic), and deoxyhaemoglobin can be magnetized by applying an external magnetic field, in the opposite direction of the external field (paramagnetic). Thus, the increase of oxyhaemoglobin concentration will reduce the local magnetic field with a corresponding increase in the MRI signal [15].

When the imaging techniques are being used, first the brain is divided into voxels, and data are recorded for each of these voxels. There are millions of neurons in each of the voxels that are collectively responsible for the observed BOLD signal. This signal oscillates with time as shown in Figure 2.3. This particular time course was acquired from a brain at rest where the subject was instructed to have eyes closed and not to be involved in any mental task.

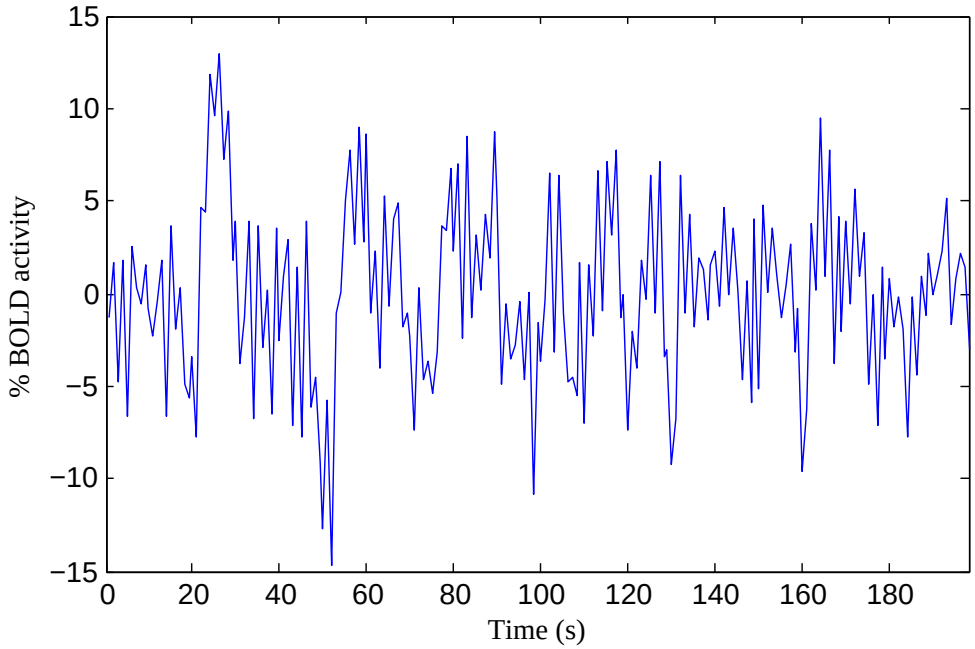

Figure 2.3: BOLD time course of a patch of cortex from a brain at rest.

2.3.2 Diffusion Tensor Imaging (DTI)

With the advent of MRI, brain imaging has benefited from sophisticated technologies. Imaging techniques have been developed with more research and, in 1994, the first measurement of the diffusion tensor in the human brain was made [16]. Following that finding, Diffusion Tensor Imaging (DTI) was developed step by step to the point that now axonal fibers can be tracked in the human brain in an accurate manner. DTI is considered a very reliable method to observe the micro-structural changes in the brain, and it is becoming a popular technique because of its high sensitivity to the changes at that level. However, there is continuous development to increase the accuracy and the spatial resolution of DTI.

The fundamental principle behind DTI is the measurement of diffusion (the microscopic random movements) of water molecules along the axonal fibers in the brain. Diffusion of water is considered because water is an essential, as well as commonly present, source in our

bodies, and 50-75% of the volume of our bodies is made up of water, reaching 75% in the brain. This huge amount of water is distributed in blood, bones and tissues in the body, but the amount of water the bones have is much less than that in blood or tissues. Due to the high abundance of water in tissues, it is a helpful substance to track down information about the micro-structure of the human body.

Water molecules diffuse as a result of thermal fluctuations. This diffusion is stimulated by an applied magnetic field gradient and at the same time by interactions with neighbouring molecules or atoms as well as interactions between molecules and cell membranes. Additionally, it is influenced by the structure of these cells containing water [17]. As diffusion depends on the structure, it is possible to visualize the diffusion of water inside the axons as well as along the fibers, giving us the opportunity to track down the path of diffusion. White matter is one type of matter in the brain which is made up of the axons of neurons in which water molecules can diffuse more freely along the fiber than across the fiber. Thus, the studies of diffusion in white matter will result in white matter tracts or fiber pathways. This kind of result could provide valuable information about the biological micro-structures of the brain [17].

Out of the several techniques available, one of the most commonly used DTI technique is pulsed-gradient, spin-echo pulse sequence, echo-planar imaging [18]. It is an MR technique that uses an additional magnetic field gradient. As described in the previous section, a strong homogeneous magnetic field is applied continuously to acquire the MR image. In DTI, the homogeneity of the magnetic field is disturbed using two magnetic field gradients of opposite directions, applied one after the other with a time delay. When the first linear magnetic field gradient is applied, the precession frequency of the protons will change depending on the magnitude of the magnetic field gradient. When it is removed, protons will have different phases. Then the next magnetic field gradient is applied with the same magnitude but in the opposite direction to refocus the phases of protons. In between the application of these two pulses, if

the protons' movement is restricted, the second gradient will allow them to be refocused to the same phase again. Thus the produced MR signal will be strong. However, if the water diffuses in this time gap, the second gradient will not be able to restore the phase shifts that have been created by the first gradient. Thus, it will produce a weak MR signal [19]. To produce a complete signal using this technique, the diffusion gradient is applied to all the x, y and z directions in DTI. Afterwards, applying the fiber tractography [20] technique to this diffusion data, the details about the physical connections in the micro-structure of the brain could be extracted. Figure 2.4 indicates the fiber tract orientation of the default mode network of the brain.

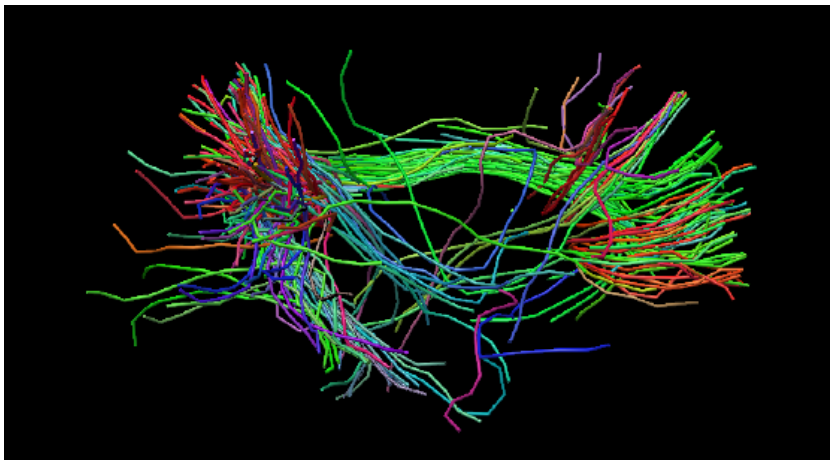

Figure 2.4: Lateral view of the white matter tracts in the brain, created by DTI. The colors, red, blue and green represent the fibers along the x, y and z directions respectively in the cartesian coordinates (DR Paula et al. in prep.)

2.4 Modelling the Brain

2.4.1 Kuramoto Model

The Kuramoto model was introduced by Yoshiki Kuramoto and used to model the synchronization of coupled phase oscillators [21]. Phase oscillators are a type of oscillator whose

states lie in the path of a circle where the phase is a variable. The model considers N number of coupled phase oscillators with natural frequencies distributed in space with a defined probability density. The model considers two states, synchronized and anti-synchronized states. In the synchronized state, all the phase oscillators, oscillate with the same frequency and in the anti-synchronized state, they oscillate with different frequencies. The objective of the Kuramoto model is to explain how the synchronized state and the anti-synchronized state of these phase oscillators can be distinguished starting with a group of unsynchronized phase oscillators. These oscillators try to oscillate with their natural frequencies, but the coupling between them always trys to synchronize the oscillations [22]. The globally coupled oscillators are defined in the model using equation 2.1:

$$\dot{\theta}_i = \omega_i + \frac{K}{N} \sum_{j=1}^{N} sin(\theta_j - \theta_i) \tag{2.1}$$

where θ_i ($\dot{\theta}_i$) and ω_i are the phase (rate of change of the phase) and the natural frequency of the i^{th} oscillator respectively, and N is the total number of oscillators in the system, while K is a constant related to the coupling in the system. There are some assumptions in the analysis of the Kuramoto model which are:

1. All the oscillators are globally coupled (each oscillator affects every other oscillator).

2. Oscillators are identical except for their different natural frequencies [23].

Using this model, it has been found that there is a critical value for the coupling in the system, and this critical value K_c, is such that for $K < K_c$ the probability of the system being synchronized is much less and when K increases past the K_c the number of oscillators synchronized increases until all of them are synchronized [24]. This critical value was able to identify a transition between an unsynchronized state and a synchronized state. However, the critical coupling constant depends on the distribution of the natural frequencies of oscillators, which adds another variability to the model.

Nevertheless, the Kuramoto model has provided a mathematical basis to model some important phenomena in real life, like simulations of neurons in the brain by modeling the observed oscillations in the BOLD signal. It is used to study some behavioural aspects of neurons because of the limited variability of the states it has. Additionally, a synchronized behaviour was also observed in neurons in the brain [25], which motivates the use of the Kuramoto model to describe the synchronization phenomena in the brain. However, the outstanding problem is that the model talks about a system that has a constant coupling parameter together with sinusoidal phase oscillations as is stated under the assumptions above. In addition to that, according to the Kuramoto model, the natural frequencies of the oscillators follow the same distribution all the time, which might not be applicable to the neural activations of the brain.

Generalized Kuramoto Model

Since the Kuramoto model was first introduced, it has been used in several areas of research, including studying biological systems like the brain. When using the Kuramoto model to model the dynamics of the brain, Deco and his group introduced some advancements to generalize the model in order to better capture the effects of structural connectivity in the brain [26]. Two changes they introduced to overcome the above indicated drawbacks and to generalize the Kuramoto model were:

1. The coupling strength between each pair of oscillators was extracted using the white matter tracks of the brain. In other words, it was extracted from the structural connectivity of the brain instead of being considered a constant.

2. The time delays of the oscillators were being scaled using the structural distance between the corresponding regions of the brain.

By applying these changes to the original Kuramoto model, Deco et al. generated a relationship between the generalized Kuramoto model and the brain without keeping it completely

isolated from the brain. Thus modelling the brain dynamics using the generalized Kuramoto model became more relevant.

2.4.2 Ising model

Two dimensional (2D) Classical Ising Model

The classical Ising model was introduced by Wilhelm Lenz in 1920. The 1D Ising model was solved by his student, Ernest Ising, in 1925, and the 2D Ising model (in the absence of an external magnetic field) was solved by Onsager in 1944 [27]. The 2D Ising model was introduced to explain the interactions of magnetic spins mathematically. The physical system (a magnet) is represented by a lattice configuration in the Ising model. Each lattice site has a spin 's' which could take only two possible values, either up (+1) or down (−1) (Figure 2.5). Thus, it is a collection of +1 and −1s representing the spins. This configuration is kept in a thermal bath of temperature T. Interactions between the spins are always influenced by this temperature and allow the system to reach an equilibrium energy state while resulting in different equilibrium spin configurations with different properties at different temperatures.

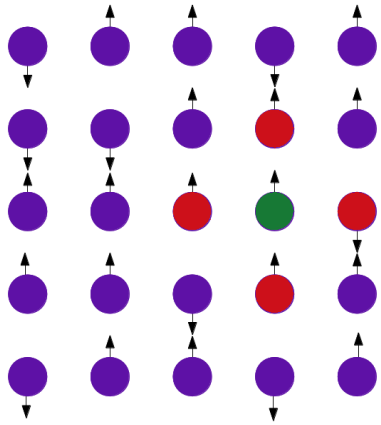

Figure 2.5: Representation of a two-dimensional lattice arrangement. Each lattice site has a spin, either up or down. The nearest neighbours of the lattice site in green are represented in red.

The energy of this spin system at any state x in the absence of an external magnetic field can be calculated using Equation 2.2:

$$E(x) = -J \sum_{i,j=nn(i)}^{N} s_i s_j \tag{2.2}$$

where J is the coupling constant, s_i and s_j represent the spins of the i^{th} and j^{th} site respectively, and N is the size of the lattice. For the calculation of energy in the Ising model, only the nearest neighbour interactions are considered together with equal coupling (J = 1). The probability of finding the system in the state x with energy $E(x)$ is given by Equation 2.3:

$$P(x) = \frac{1}{Z} \, e^{-\frac{E(x)}{k_B T}} \tag{2.3}$$

where k_B is the Boltzmann constant, T is the temperature of the heat bath and Z is the partition function. Equation 2.4 illustrates the partition function of the system which describes the statistical properties of the spin system in thermodynamic equilibrium. The summation is over

all possible 2^N spin configurations.

$$Z = \sum_{\{x\}} e^{-\frac{E(x)}{k_B T}} \tag{2.4}$$

When a 2D lattice configuration is considered, there are two extreme equilibrium configurations of spins it can hold, one for lower temperatures and the other one for higher temperatures. When the temperature is very low, all the spins can be aligned along the same direction, with very large clusters of the same spin, either up or down (ordered) resulting in high magnetization even in the absence of an external magnetic field (Figure 2.6 (a)). In the other end, when the temperature is very high, the spins are a mixture of up spins as well as down spins (disordered) without any order which will result in zero magnetization (Figure 2.6 (c)). In between these two extremes of temperature, there exists a critical temperature (T_c) [3] where the system exhibits transition from ordered phase to the disordered phase (Figure 2.6 (b)). As the figure illustrates, at this temperature there is a mixture of ordered spins as well as disordered spins. Additionally, the system acquires its maximum susceptibility or the maximum change in magnetization at T_c. Even a single spin flip can change the entire system [28], and the perturbation introduced by a single spin flip can spread over the entire system rapidly. Therefore, with different temperatures of the heat bath, the system could exhibit completely different properties [27] which depend only on the temperature of the system.

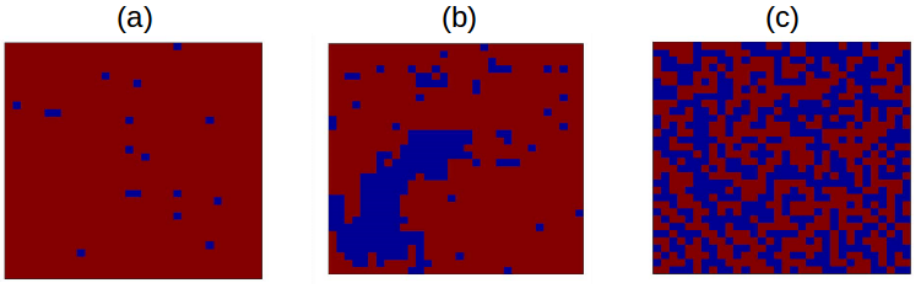

Figure 2.6: Representation of the equilibrium spin configuration for (a) $T < T_c$, (b) $T = T_c$ and (c) $T > T_c$ for a two-dimensional lattice arrangement. Red color is for the up spins (+1) and blue color is for the down spins (−1) [3].

To simulate the dynamics of the classical Ising model, the Metropolis Monte Carlo algorithm is used. The Metropolis algorithm involves the construction of a new state based on the current state of the system with a transition probability. It is used in the Ising model to find the equilibrium energy state starting from a random spin configuration for a constant temperature. Monte Carlo simulations are used to describe or to solve systems which change in time without any predefined dynamical pattern but depending on random numbers created along the simulations [29]. These algorithms are used in the classical Ising model with the periodic boundary conditions. Periodic boundary conditions were introduced to the system to restrain the finite size effects. The application of these algorithms in order to construct the equilibrium spin states, and then the time fluctuations of the spins for a range of temperatures, will be discussed in detail in the methodology section (Chapter 3).

An important question that arises next is why it is possible to use the dynamics of the Ising model which were introduced by using the Metropolis Monte Carlo algorithm to explain the dynamics of the brain. In the simplest way, spins of the Ising model can be considered as equivalent to the BOLD activity in the brain with +1 for the activity higher than the baseline activity and −1 for the activity lower than the baseline activity. Additionally, it is a very sim-

ple model that explains the phase separation. Furthermore, Fraiman et al. [30] state the Ising model can be used to explain the behaviour of the brain at the critical temperature because of the similarities it has shown in its dynamics and the brain's spatio-temporal patterns. The classical Ising model exhibits long range correlations at the critical temperature, which explains the observed interactions of the spins that are spatially distant from each other. This fact can be compared with the functional integration observed in the brain. The brain maintains a balance between the functional integration and segregation in order to perform efficiently. As observed in the behaviour of the brain, there are separate regions which are specialized to perform certain functions. While functioning separately, these regions need to exchange information with each other in order to function as a complete system. This process is explained as the functional integration and can be compared with the long range correlations observed in the Ising model. Thus the classical Ising model was chosen to model the oscillations observed in BOLD signal for comparison.

Generalized Ising model

The generalized Ising model is an advancement from the classical Ising model. The generalization was performed by including the information related to the structure of the brain in the classical Ising model following the work of Marinazzo et al. [31]. They implemented the generalized Ising model by using the structural connectivity of the brain, without introducing the dynamics to the spins variables. By analysing the results they claimed that, the total information transfer between spin variables in the model is maximized at the critical state. Similarly, we implement the generalized Ising model using the structural connectivity; but in addition, we introduce the dynamics to the spins using the Metropolis Monte Carlo algorithm. The methodology will be discussed in details in Chapter 3. However, there are two differences between the classical Ising model and the generalized Ising model.

1. According to the generalized Ising model, all the lattice points are interacting with all the other lattice points with different strengths. This is true in the sense of the structure of the brain. In the brain, there are some regions that are highly structurally connected with larger numbers of fibers and some regions that are poorly connected.

2. When using Equation 2.5 to calculate the energy of the system, normalized structural information is used for J_{ij} instead of equal coupling as in the classical Ising model (explained in detail in Chapter 3). Due to this modification, the strength of connection held between two regions is taken into account by the generalized Ising model.

These two points are illustrated in Equation 2.5:

$$E(x) = -\sum_{i,j;i\neq j}^{N} J_{ij} s_i s_j \tag{2.5}$$

where J_{ij} is the coupling constant between the i^{th} site and the j^{th} site. The summation is over all the sites, without the restriction of the nearest neighbour coupling as in the classical Ising model.

However, due to these two modifications, the spin sites in the generalized Ising model has a one-to-one relationship with the patches of cortices in the brain. Hence, it could be used to study the dynamics of the brain not only on a global level, but also on a local level. Nevertheless, the classical Ising model, as described earlier, is a 2-dimensional model, and each spin site has four nearest neighbours. But in the generalized Ising model, we propose that each region is connected with every other region, resulting in each site having n - 1 (number of regions - 1) nearest neighbours. This makes the model more realistic because, as it is understood from the structural connectivity data of the brain, there are connections between most of the regions and not just between the nearest neighbours. Notice that, the dimension of the generalized Ising model is unknown. However, in order to extract the effective dimension of the model, the

critical exponents could be studied at the criticality.

All the observables in the classical Ising model behave according to the Equation 2.6 when reaching the critical temperature, as explained by Lilian and Manuel in [32]:

$$O(T) \propto | \frac{T - T_c}{T_c} |^{\alpha} \tag{2.6}$$

where $O(T)$ is any observable, α is the critical exponent and T_c is the critical temperature. Thus, we could find the critical exponents for all the observables, such as the magnetization, magnetic susceptibility, specific heat, correlation function and correlation length. Those critical exponents should follow the scaling relations given in Equation 2.7 as described in [32]:

$$\begin{aligned} (2 - \eta)\nu &= \gamma \\ \frac{\nu}{2}(\eta + d - 2) &= \beta \\ 2 - \nu d &= \alpha \end{aligned} \tag{2.7}$$

where $\beta, \gamma, \alpha, \eta, \nu$ are the critical exponents of magnetization, magnetic susceptibility, specific heat, correlation function and correlation length, while d is the dimension of the system. Therefore, by extracting the critical exponents of the generalized Ising model, we will be able to find the dimensionality d of the generalized Ising model (Das et al., in prep.) using the above scaling relations.

2.4.3 Generalized Kuramoto Model versus Generalized Ising model

As explained in the previous sections, the Kuramoto model takes a network of coupled oscillators into account and finds a critical point in between the unsynchronized and synchronized states of these coupled oscillators. The Ising model takes a spin configuration into account and finds a critical state where the phase transition of the spins occurs from the ordered to disor-

dered phase. Both of these phenomena at the critical states are compared with the dynamics of the brain even though there is no one-to-one relationship between either of the oscillator or the spin lattice sites and the position of the patch of cortex in the brain.

Sometime after the introduction of the Kuramoto model, it was generalized such that the coupled oscillators represent the structural regions of the brain, as described in section 2.4.1. The generalized Kuramoto model could give a detailed explanation of the functional networks of the brain, starting with the structural connectivity [33]. However, as Deco et al. [26] explained in the paper, the generalized Kuramoto model still has four main free parameters, which are mean delay, global coupling strength and two standard deviations from two Gaussian distributions (one modelled for the dispersion of oscillation frequencies and the other one modelled for the noise of the local networks). Similarly, we are generalizing the Ising model using the anatomical structure of the brain in place of the constant coupling in the classical Ising model; but the model has only one controlling parameter, the temperature of the heat bath.

2.5 Graph Theory

Graph theory is a mathematical tool that can be used to study networks with complex topologies. It reveals important information about the connectivities in terms of single units and sub groups as well as a complete network. Graph theory has been used broadly to study highly complex networks like the internet and air craft flight patterns as it is a simple tool, which explains the complexity of the subjected networks. Therefore, we use graph theoretical analysis of the complex brain network. In this context, a graph is a network with source nodes and edges that connect the nodes. Using graph theory to analyse the complex network of the brain simplifies the analysis and provides a more general understanding. As Bullmore and Sporns reviewed [34], the increasing demand of analysing more complex network structures is very

well handled by the use of graph theory. The equivalent of an edge in a graph could be explained by a structural or functional connection in the brain network and a node by a region or a collection of regions in the brain. There are several measures in graph theory being used to study this complex connectivity.

The degree of a node in the network is one of the simplest measures. It is defined as the number of links a node has and can be calculated using Equation 2.8:

$$k_i = \sum_{j \epsilon N} a_{ij} \tag{2.8}$$

where k_i is the degree of the i^{th} node, N is the number of nodes in the network and a_{ij} is the connection status between the i^{th} node and the j^{th} node (it is equal to 1 if the nodes are connected and 0 if they are not, in a binary network) [35]. The degree averaged over all the nodes is defined as the global degree of that network. An understanding about how dense or sparse the network is could be gained from the average degree of the network.

Following that, we calculated the efficiency for these networks, which is discussed as a measure of functional integration. The global efficiency of a binary network can be calculated using Equation 2.9:

$$EFF = \frac{1}{n} \sum_{i \epsilon N} EFF_i = \frac{1}{n} \sum_{i \epsilon N} \frac{\sum_{j \epsilon N,\, j \neq i} d_{ij}^{-1}}{n-1} \tag{2.9}$$

where EFF_i is the local efficiency, d_{ij} is the shortest path length between nodes i and j and n is the total number of nodes in the network [36]. The efficiency of a network provides an understanding about the information propagation through the network, or in other words, the ability of the network to handle information integration.

Equation 2.10 was used to calculate the small-world property for each network:

$$S = \frac{C/C_{rand}}{L/L_{rand}} \tag{2.10}$$

where C and C_{rand} are the clustering coefficients, and L and L_{rand} are the characteristic path lengths of the network being tested and a random network respectively. A random network is created by preserving the degree distribution of the tested network. Small-world networks are characterized by the average short path lengths and high clustering coefficients [37]. It is a measure of the balance between information integration and segregation. Average path length is a measure of integration which is defined as the average of shortest distance between each pair of nodes. Clustering coefficient is a measure of the segregation or in other words it measures the tendency of the nodes to cluster together. In neuroscience, it has been shown in several analyses that the brain network shows small-world network properties, implying that it maintains a balance between integration and segregation. Small-world networks often have values greater than 1 for S [38, 35]; but the value of S could easily be misinterpreted without knowing about the connectivity of the network. For an example, the average path length can be very small for networks with lower number of edges and lower number of participating nodes. Although the clustering coefficient can be high for these type of networks because of the small number of nodes in the network. This can result in higher small-world property which stands for an efficient network with a well balanced information integration and segregation.

Chapter 3

Methodology

3.1 Overview

In this chapter, we focus on the procedure for generating the two types of data sets we used: brain data and simulations. In the first section, we would like to focus on the method of extraction of the functional brain data from fMRI. The methodology used for the acquisition and extraction of structural data using DTI will then be explained, followed by a section with a detailed explanation of numerical simulations of the models. The acquisition and preprocessing of fMRI data and DTI data was performed by Erik Ziegler (University of Liege, Liege, Belgium). In section 3.3, we will describe the methodology for the simulation of the generalized Ising model. The simulations of the classical Ising model will be described after that followed by a description of the methodology used for the analysis of these data.

3.2 Empirical Data from MRI

3.2.1 Subjects

For the collection of data, 14 healthy subjects with mean age 43 ± 15 were studied, including seven women. The study was approved by the Ethics Committee of the Medical School of the

University of Liege. In addition, informed approval to participate in the study was obtained from all the subjects. From these healthy subjects, the resting state fMRI (rsfMRI) and DTI data were acquired and preprocessed using the methods described below.

3.2.2 Acquisition & Preprocessing

Functional Data

Resting state BOLD data were acquired on a 3-T MR scanner with a gradient-echo echo-planar imaging sequence using axial slice orientation and covering the whole brain (32 slices, voxel size: $3 \times 3 \times 3$ mm^3; matrix size $64 \times 64 \times 32$; repetition time = 2000 ms; echo time = 30 ms; flip angle = 78^0). Data preprocessing was performed using Statistical Parametric Mapping (SPM) 8 (www.fil.ion.ac.uk/spm). Preprocessing steps included realignment and adjustment for movement related effects, co-registration of functional images with structural images, segmentation of structural data, spatial and functional normalization and spatial smoothing of the fMRI data.

Segmentation of images for each subject was performed with the FreeSurfers Desikan-Killiany atlas [39]. This atlas provides the ability to separate the brain into gyral-based regions of interest (ROI) automatically. Thus using the atlas, the images could be segmented. Further parcellation, using the Lausanne 2008 atlas and its 83 individually labelled regions, was done with functions from the Connectome Mapping Toolkit [40, 41, 42]. The labels of the 83 regions are presented in Appendix C followed by a figure representing the 83 regions (Figure .3).

Structural Data

Diffusion Weighted Images (DWI) were acquired from each subject, and the Fractional Anisotropy (FA) maps which quantify diffusion-weighted effects at the voxel level were generated. After

that, orientation distribution functions were obtained for each voxel. Probabilistic tractography [43] was performed throughout the whole brain using randomly placed seeds inside a subject-specific white-matter mask. The set of points representing each fiber track were then affine-transformed into the subjects' structural spaces which results in the connectivity maps. Finally, connectivity matrices with the number of fibers connecting each of the 83 regions with all the others were obtained for 14 subjects, and the normalized mean connectivity was used as an input of the generalized Ising model.

3.2.3 Resting State Network (RSN) extraction

After using Independent Component Analysis (ICA) [44] for BOLD decomposition in an independent data set of 19 healthy controls, nine Resting State Networks (RSNs) were identified in each subject, and an average template was created for each RSN. Subsequently, by setting a separate threshold for each RSN, the region of interests (ROIs) out of the 83 parcellated regions belonging to the network were extracted. Extracted ROIs for each network are presented in Appendix D. Finally, the lines of the correlation matrix corresponding to each ROI for the same RSN were averaged in order to obtain the linear-correlation maps plotted in Figure 4.9.

3.3 Numerical Simulations

3.3.1 Generalized Ising Model

The generalized Ising model was developed by starting with a 1D-random spin configuration of lattice of size 83, which is assumed to be in contact with a thermal bath of temperature T. The steps below have been followed according to the Metropolis Monte Carlo algorithm to obtain the equilibrium spin configuration, for a particular temperature starting with random spin states. The connectivity matrix used for the simulation of the generalized Ising model is presented in Figure 3.1 (c).

1. A random spin configuration was defined with the lattice size of 83.
2. Initial energy E_{in} of the system was calculated using Equation 2.5.
3. Next, one spin was selected randomly from the spin configuration and was flipped.
4. The new energy E_{new} was calculated.
5. Then E_{in} and E_{new} were compared.
    - If $E_{new} < E_{in}$, the spin flip was accepted and the new configuration was considered the initial configuration with $E_{in} = E_{new}$. Then the simulation was continued starting from Step 3.
    - If $E_{new} > E_{in}$, the Boltzmann factor $B = e^{-\frac{\Delta E}{k_B T}}$ was calculated and a random number r was drawn from a normal distribution. Then these two values were compared.
        - If $B > r$, the spin flip was accepted and E_{in} was replaced with E_{new}. Then the procedure was repeated starting from Step 3.
        - If $B < r$, the spin flip was rejected, and the simulation was started over from Step 3.

The steps starting from Step 3 were repeated until we obtained an equilibrium spin configuration with an equilibrium energy for a particular temperature. At the equilibrium state, energy of the system fluctuates within a small range. The random configuration can evolve into this state by following single-spin-flip dynamics as explained in the algorithm. This equilibrium configuration was considered as the configuration at time $t = 0$. After that, by following the Metropolis Monte Carlo simulations, the time evolution of the equilibrium spin configuration was obtained as follows;

- Equilibrium spin configuration = the configuration at time t = 0.

- Next, all the spins in the configuration were tested for flip by flipping one at a time and comparing E_{in} and E_{new} to decide whether to accept or to reject the flip using the Metropolis Monte Carlo algorithm. After all the spins had been checked, the new configuration was considered the configuration at time t = 1.

- After that, all the spins of this new configuration were checked for flip as in the previous step. When all the spins had been checked, the new configuration was taken as the configuration at time t = 2.

- These steps were repeated until we found as many time points as needed to compare with the empirical data.

By the end of this process, the time evolution of the spins for each spin site was obtained. Using these time series data, and Equation 3.1, the correlation between each pair of sites in the lattice was calculated:

$$\rho_{ij} = \frac{< s_i(t)s_j(t) > - < s_i(t) >< s_j(t) >}{\sigma_{s_i(t)}\sigma_{s_j(t)}} \tag{3.1}$$

where ρ_{ij} is the correlation between the i^{th} and j^{th} spin time series, $s_i(t)$ and $s_j(t)$ stands for the spin time courses of the i^{th} and j^{th} region, $\sigma^2_{s_i(t)} = < s_i^2(t) > - < s_i(i) >^2$ and $< . >$ is the average over time.

Starting from a random configuration, this complete procedure was repeated for different temperatures "T" ranging from 0.5 to 3 in increments of 0.01. Additionally, k_B was equated to one, in the simulations. This was repeated for ten iterations, and data were recorded separately each time. We performed the simulation for ten iterations to observe the effect of randomization of the spins at the first step of the simulations. An illustration of the variation with respect to the iteration is presented in Figure .1 in the Appendix B.

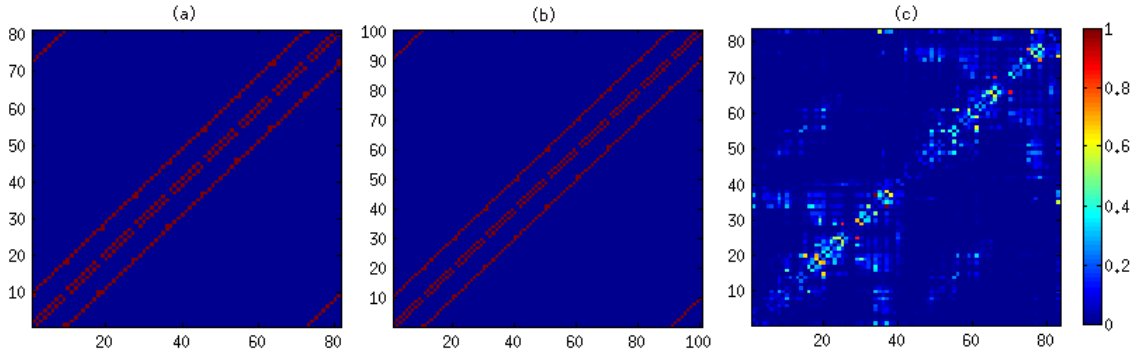

Figure 3.1: Connectivity matrices used for the simulations of the classical Ising model (a) 9 × 9 , (b) 10 × 10, and (c) the generalized Ising model.

During these simulations, the energy (E), magnetization (M) and susceptibility (χ) of the system were calculated using Equations 2.5, 3.2 and 3.3 respectively at each temperature:

$$M = \frac{1}{N}\sum_{i=1}^{N} s_i \tag{3.2}$$

$$\chi = \frac{1}{NT}[< M^2 > - < M >^2] \tag{3.3}$$

where N = 83 and s_i is the spin of the i^{th} region. Derivation of Equation 3.3 is presented in [45]. These quantities were plotted as a function of temperature, and the susceptibility versus temperature plot was used to extract the critical temperature (T_c), which gives the highest susceptibility. Super critical ($T > T_c$) and sub critical ($T < T_c$) temperatures were chosen relative to the critical temperature. The MATLAB code which was used for the simulations of the generalized Ising model is attached in Appendix A.

3.3.2 2D Classical Ising Model

The classical Ising model was developed by following the same steps, and using Equation 2.2 instead of Equation 2.5 to calculate energy, which includes equal coupling as well as only the

nearest neighbour interactions. The 2D Ising model was simulated using two lattice sizes 9×9 (L = 9) & 10×10 (L = 10) which result in 81 and 100 spin sites respectively. These two sizes were chosen to make the 2D Ising model comparable with the empirical data, which has 83 spin sites. Given this choice, two separate data sets were obtained for each lattice size with temperature ranging from 0.5 to 4. The connectivity matrix used for the simulations of the classical Ising model is presented in Figure 3.1 (a) and (b).

In a similar manner, Equations 3.2 and 3.3 were used to calculate the magnetization and susceptibility of the system, where $N = L \times L$ in the classical Ising model. After extracting the critical temperature for both of the lattice sizes, those values were verified using Equation 3.4 [32]:

$$T_c = (20.28) \times \frac{1}{L^2} + 2.26 \tag{3.4}$$

where L is the length of the square lattice (either 9 or 10).

3.4 Comparison of data

As explained in the previous sections, the functional correlation was obtained for the regional parcellation of 83 regions in the brain using rsfMRI, which will be hereafter called the empirical data. The structural connectivity was obtained by the extraction of white matter tracts from DTI. In addition to that, we generated three sets of data from the mathematical simulations of the Ising model: one from the generalized Ising model using the structural connectivity, and the other two sets from the classical Ising model for two different lattice sizes.

The mean data over the ten iterations were considered to perform our analysis. A comparison of the correlations of the empirical data, generalized Ising model data and the classical Ising model data was performed first. After observing the correlation maps for three different temperatures, we calculated the Kolmogorov Smirnov (KS) test statistic at each temperature

to find the temperature which minimizes the distance between two cumulative distributions for each model. KS test is a non-parametric test which has been used to test two distributions. The test statistic calculates the maximum distance between two cumulative distributions and this has been used to find the temperature which minimizes the distance between two distributions in our data. Thereafter, graph theoretical measures as explained in Chapter 2 have been used to compare the classical Ising model and generalized Ising model data with the empirical data. The results will be presented in the next chapter.

Chapter 4

Results

4.1 Overview

In this chapter, we will present our results obtained using the methodology explained in Chapter 3.

4.2 The Classical Ising model versus the Generalized Ising model

Three correlation data sets were obtained by following the procedure explained in Chapter 3. During the process of creating these, the energy, magnetization and susceptibility of the systems were calculated as a function of temperature. Hence, these quantities were plotted for the classical Ising model, as well as for the generalized Ising model, as shown in Figure 4.1.

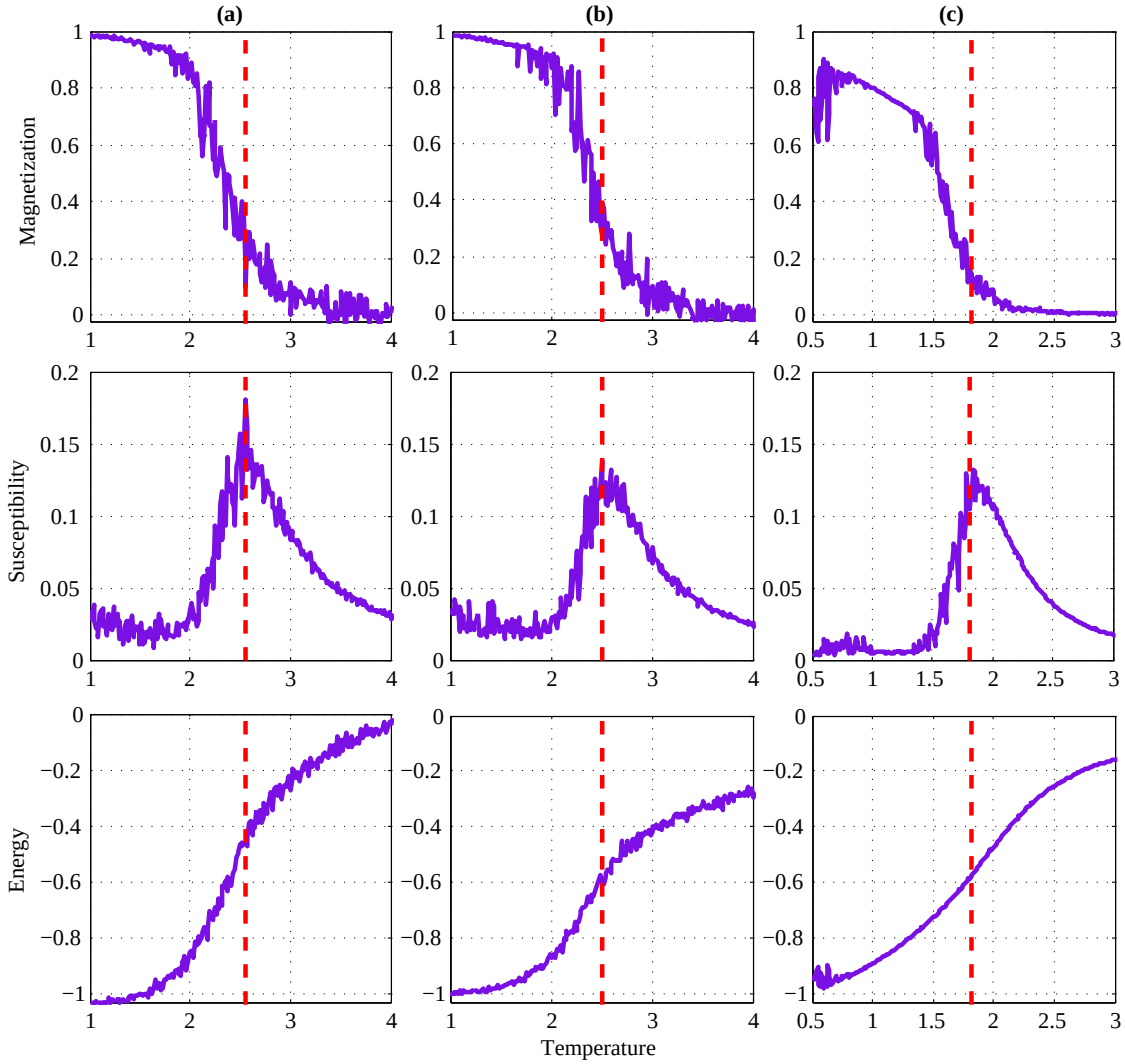

Figure 4.1: Magnetization, susceptibility and Energy as a function of temperature for the Classical Ising model with (a) 9×9 and (b) 10×10 lattice size, and (c) the Generalized Ising model. Red dashed line indicates the T_c.

The critical temperature was extracted in both models using the susceptibility versus temperature plot (second row of the Figure 4.1). Relative to the critical temperature, a sub-critical and a super-critical temperature was selected such that for both of the models the selected temperatures maintain the same distance with the critical temperature (Table 4.1).

The equilibrium spin configurations were then obtained by following the Metropolis Monte

Model	$T < T_c$	$T = T_c$	$T > T_c$
Generalized Ising model	0.64 ± 0.06	1.79 ± 0.06	2.89 ± 0.06
Classical Ising model (9 × 9)	1.40 ± 0.10	2.55 ± 0.10	3.65 ± 0.10
Classical ising model (10 × 10)	1.35 ± 0.06	2.50 ± 0.06	3.60 ± 0.06

Table 4.1: Extracted temperature values for the three cases in the two models

Carlo Algorithm, and used to calculate the correlations among the spin sites. An illustration of the correlations relative to the extracted three temperatures is presented in Figure 4.2 for the classical Ising model and for the generalized Ising model.

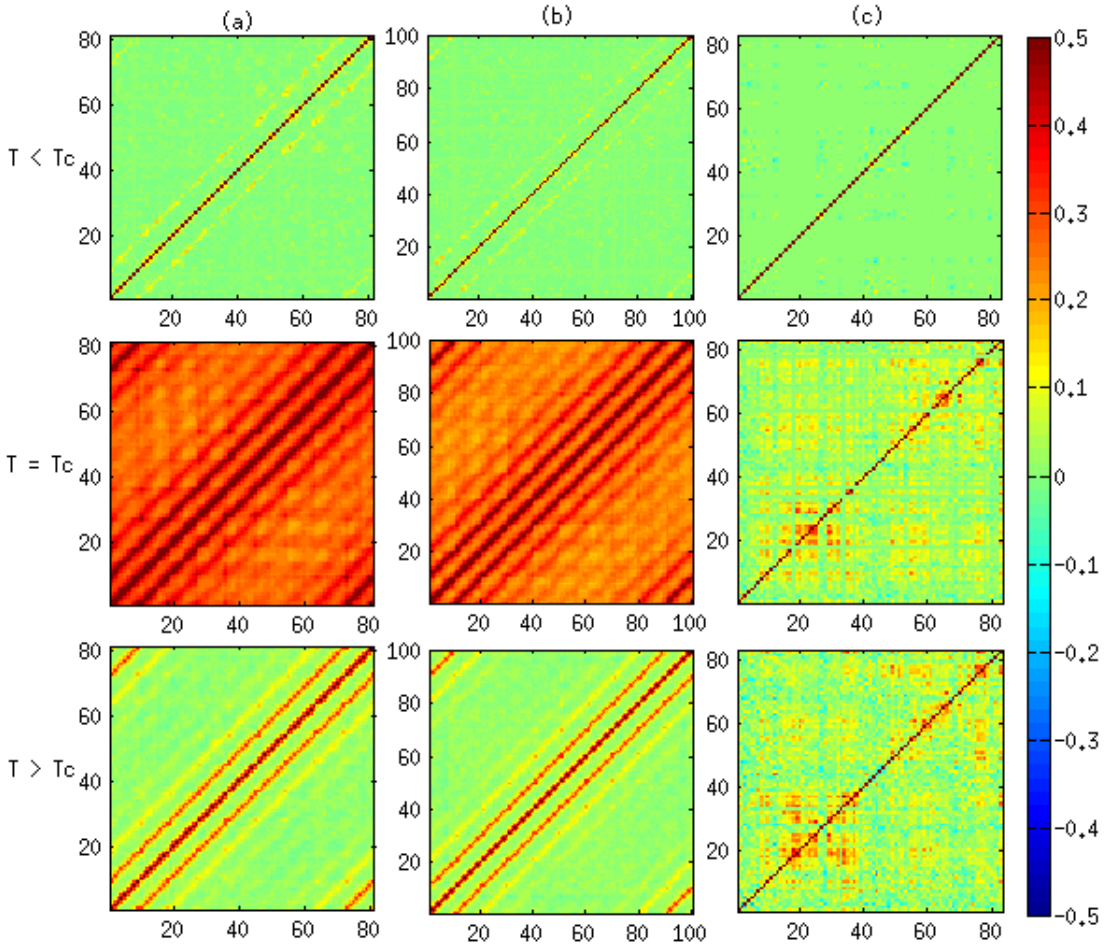

Figure 4.2: Correlation at $T < Tc, T = Tc$, and $T > Tc$ for the classical Ising model with (a) 9 × 9 and (b) 10 × 10 lattice sizes, and (c) the generalized Ising model.

As the correlation matrix of the generalized Ising model at T_c did not match with the empirical correlation matrix, another temperature was calculated using the well known KS test as explained in the methodology. Figure 4.3 illustrates the KS test statistic which calculates the distance between the distributions of the correlation for the empirical data, and the simulated data at different temperatures, for the classical Ising model and for the generalized Ising model as a function of temperature. Using these three plots, a new temperature T^*, which minimizes the distance between two distributions of data was extracted for each model. T^* for the classical Ising model for 9×9 was 2.63 and for 10×10 was 2.58, and T^* for the generalized Ising model was 2.02.

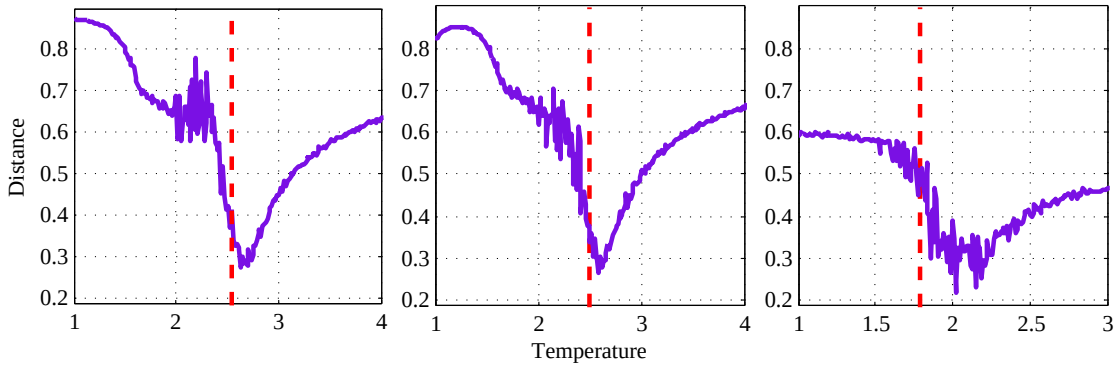

Figure 4.3: KS test statistic for the classical Ising model with (a) 9×9 and (b) 10×10 lattice sizes and (c) the generalized Ising model as a function of temperature. Red dashed line indicates the critical temperature for each model.

The simulated correlation matrices for the classical Ising model and for the generalized Ising model at T^* are shown in Figure 4.4.

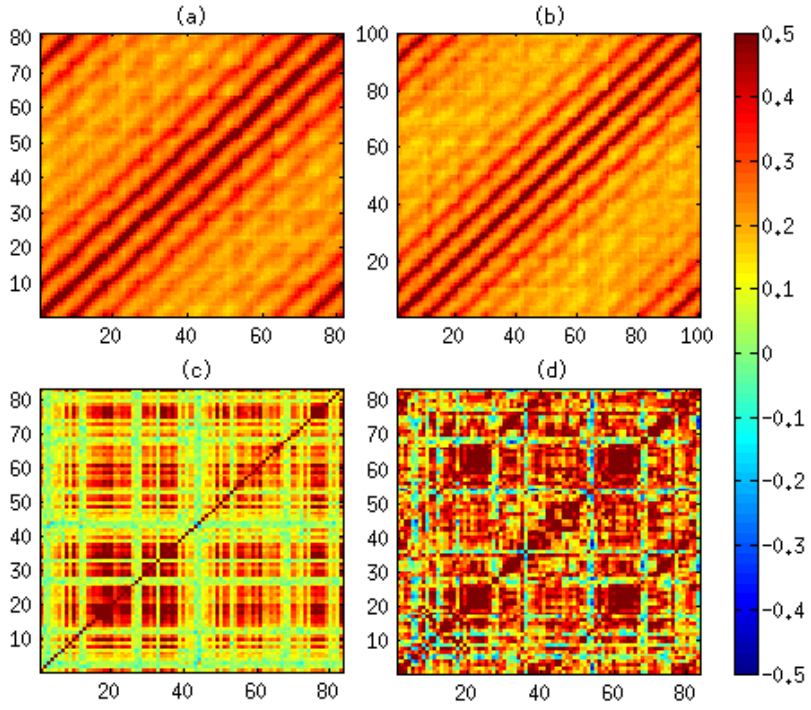

Figure 4.4: Simulated correlation matrices at T^* for the classical Ising model with (a) 9×9 and (b) 10×10 lattice sizes and (c) the generalized Ising model together with (d) the empirical correlation matrix.

After determining T^*, the distributions of correlations with respect to the extracted four temperatures were plotted and are presented in Figure 4.5 with the distribution of correlation for the empirical data. In the classical Ising model, correlation values at both the critical temperature and T^* is similar to the empirical data even though they did not show a similarity of the pattern in the correlation maps. For the generalized Ising model, correlation map at T^* is more comparable with the empirical data in terms of the values of correlations as well as the pattern observed in the correlation map.

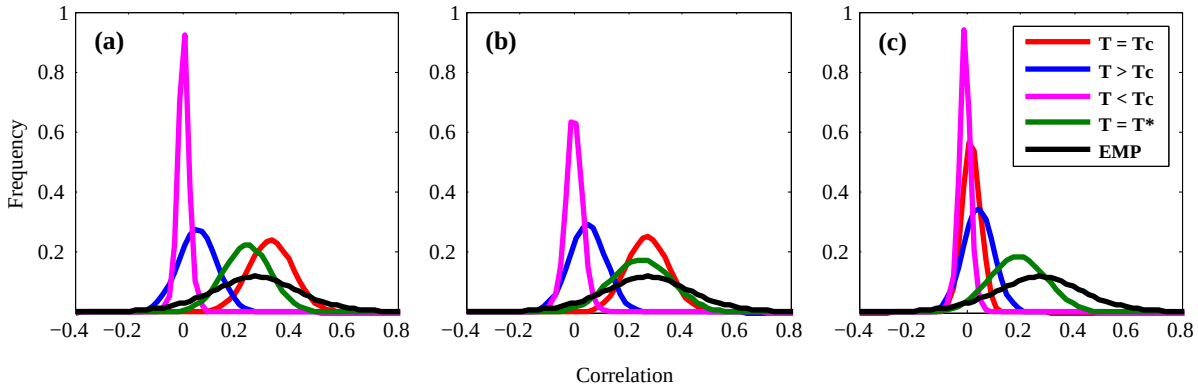

Figure 4.5: Distribution of the correlation at $T < T_c, T = T_c, T > T_c$ and $T = T^*$ for the classical Ising model with (a) 9×9 and (b) 10×10 lattice sizes, and (c) the generalized Ising model with the distribution of the correlation for empirical data (EMP). The frequency in the y-axis is the normalized frequency.

Graph theoretical properties, such as the global degree and the global efficiency were calculated as explained in the method section for these three types of data, after creating the connectivity matrices. A range of thresholds were selected at first to create the connectivity matrices. In Figure 4.6, the global degree is plotted as a function of the selected thresholds for the positive and negative correlations with respect to the two models. When the positive correlation is considered, the generalized Ising model shows a similar behaviour to the empirical data at T^*. However, the average degree of the positively correlated networks at T_c or T^* in the classical Ising model deviates from that of the empirical data than the generalized Ising model.

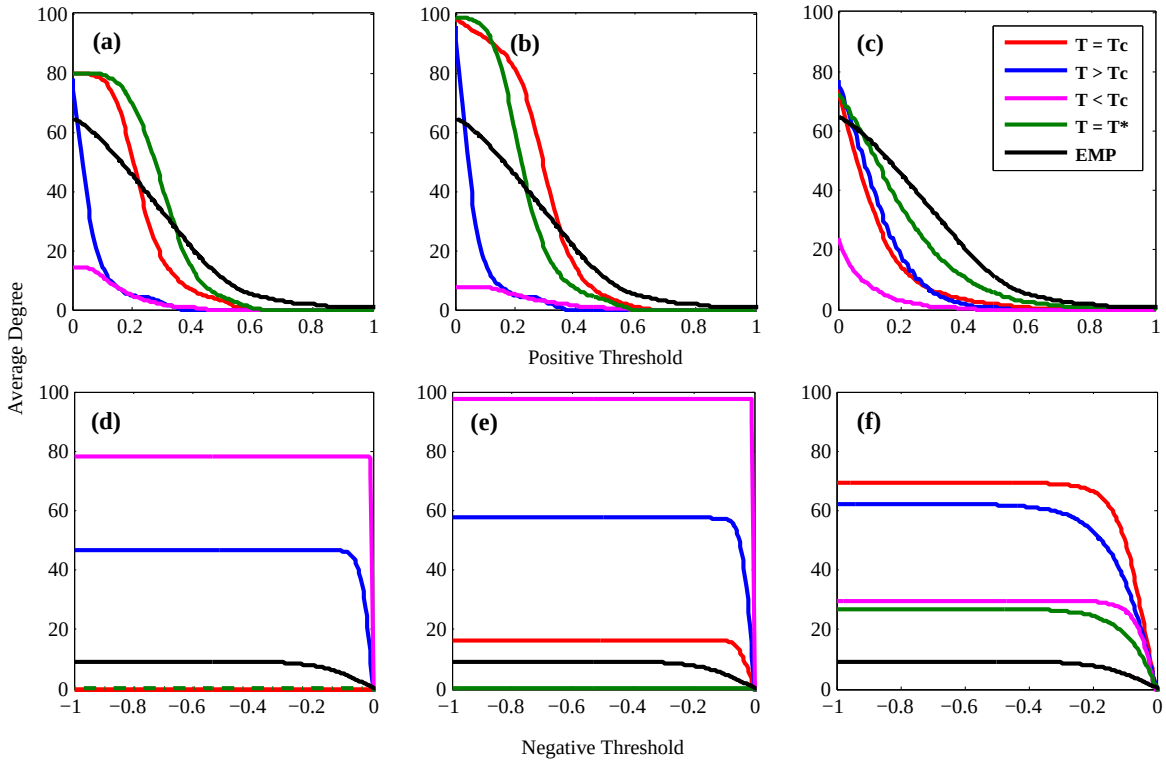

Figure 4.6: Variation of the average degree as a function of the threshold. Top three panels give the average degree with positive correlation for the (a) Classical Ising model: 9×9, (b) Classical Ising model: 10×10 and (c) Generalized Ising model. The bottom three panels show the average degree for the negative correlation for (d) Classical Ising model: 9×9, (e) Classical Ising model: 10×10 and (f) Generalized Ising model.

The correlations were binarized after selecting a threshold, and the global degree and global efficiency were calculated for a binary graph as a function of temperature (Figure 4.7). These quantities were plotted for three different thresholds along with the results from the empirical data. It is evident in these plots, for the generalized Ising model the maximum average degree and the efficiency were obtained near the T^* value. For the classical Ising model, the maximum values were obtained near the critical temperature. In these figures, the same quantities for the empirical data are plotted as straight lines for the three different thresholds.

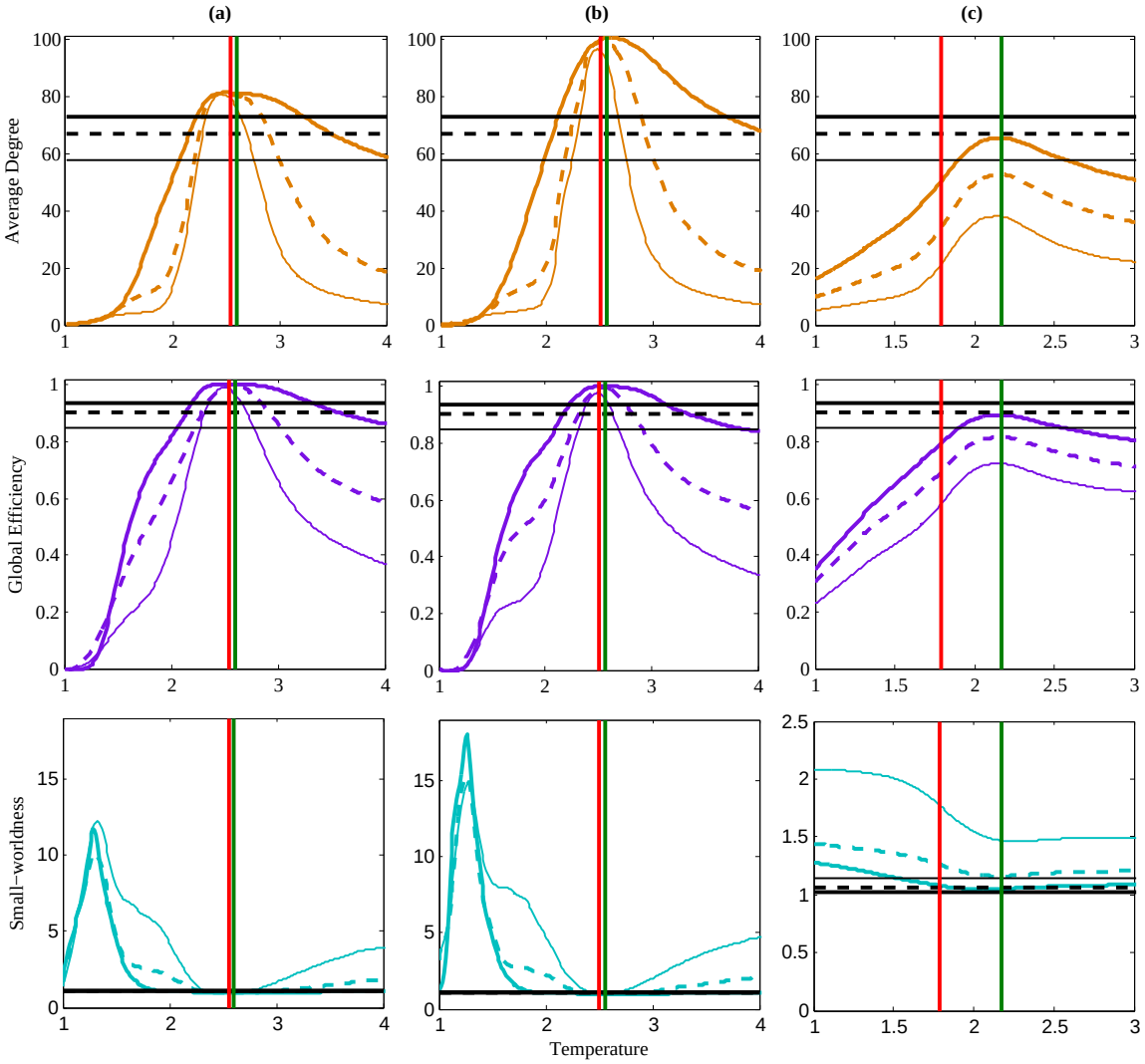

Figure 4.7: Graph theoretical properties as a function of temperature for the classical Ising model with (a) 9×9 and (b) 10×10 lattice sizes, and (c) the generalized Ising model. The thick solid line represents threshold = 0, the dashed line represents threshold = 0.07 and the thin solid line represents threshold = 0.14. The black lines represent the properties of the empirical data for the above thresholds. The red and green vertical lines represent the T_c and T^* respectively.

In Figure 4.8, the connectivity graphs of these networks, which were extracted from the generalized Ising model, have been plotted for the four temperatures along with the empirical brain network. These maps were created by binarizing the correlation matrices at each temper-

ature by applying a threshold. That allows to determine which regions are connected and which are not connected. In these graphs, each point represents a brain region and in this study there were 83 regions. It can be seen that the connectivity in the network grows as the temperature reaches T^* and has reduced at $T > Tc$. Furthermore, when the euclidean distances between these four graphs and the empirical graph were calculated, the connectivity graph at T^* resulted the lowest distance of 5.1 while the distances for the graphs at $T < T_c$, $T = T_c$ and $T > T_c$ resulted in 8.1, 7.1 and 7.0 respectively. The connectivity graphs could not be implemented for the classical Ising model as there was no one-to-one match between the regions of the classical Ising model and the regions of the brain.

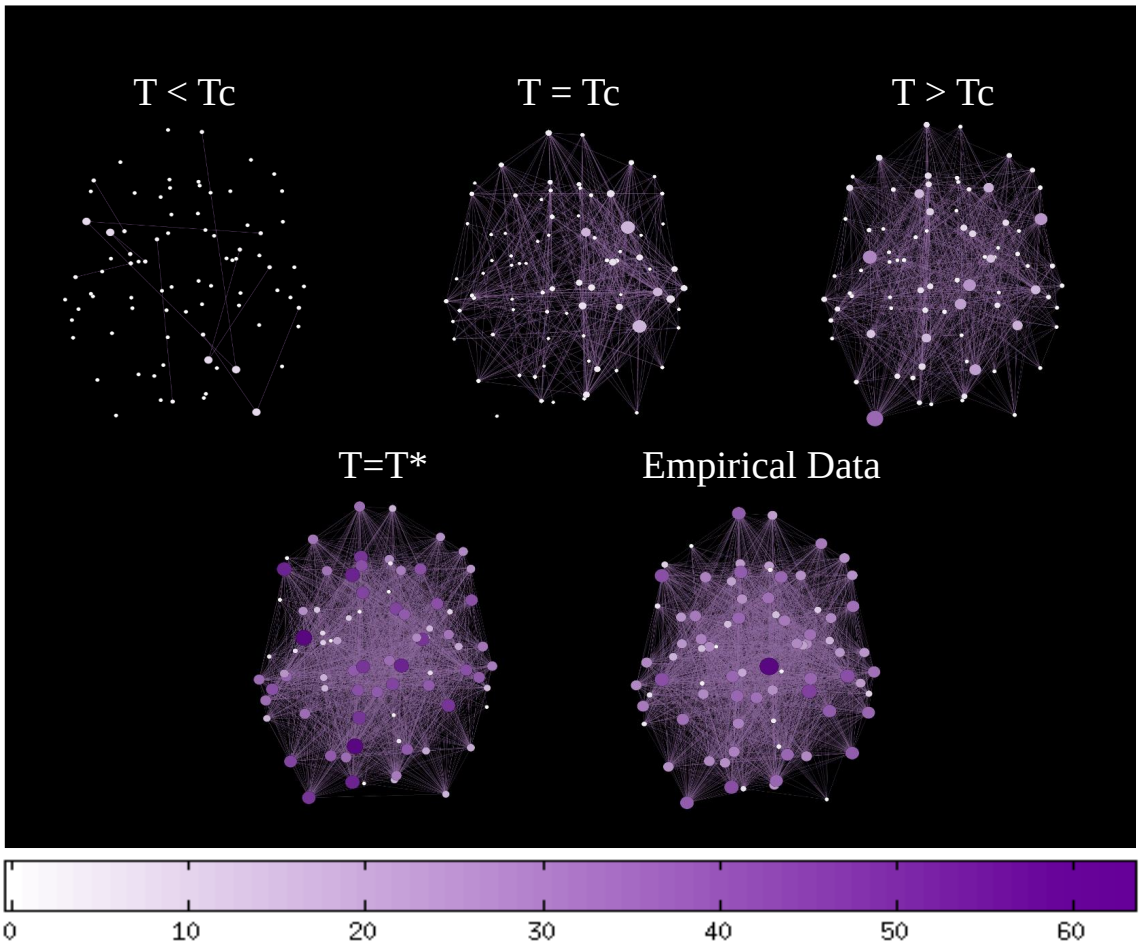

Figure 4.8: Connectivity graphs for the generalized Ising model for four temperatures, along with the connectivity graph of the empirical network, thresholded at 0.07. The color and the size of the nodes represent the degree. The darker the color and larger the size, the higher the degree of each node in the network.

Figure 4.9 illustrates the correlation maps of the 9 RSNs extracted from the generalized Ising model for four different temperatures, as well as the RSNs extracted from the empirical data. From these maps, it is evident that the correlation of the corresponding regions of each network emerges from the generalized Ising model at T^* rather than at T_c as observed in the brain maps of the empirical data.

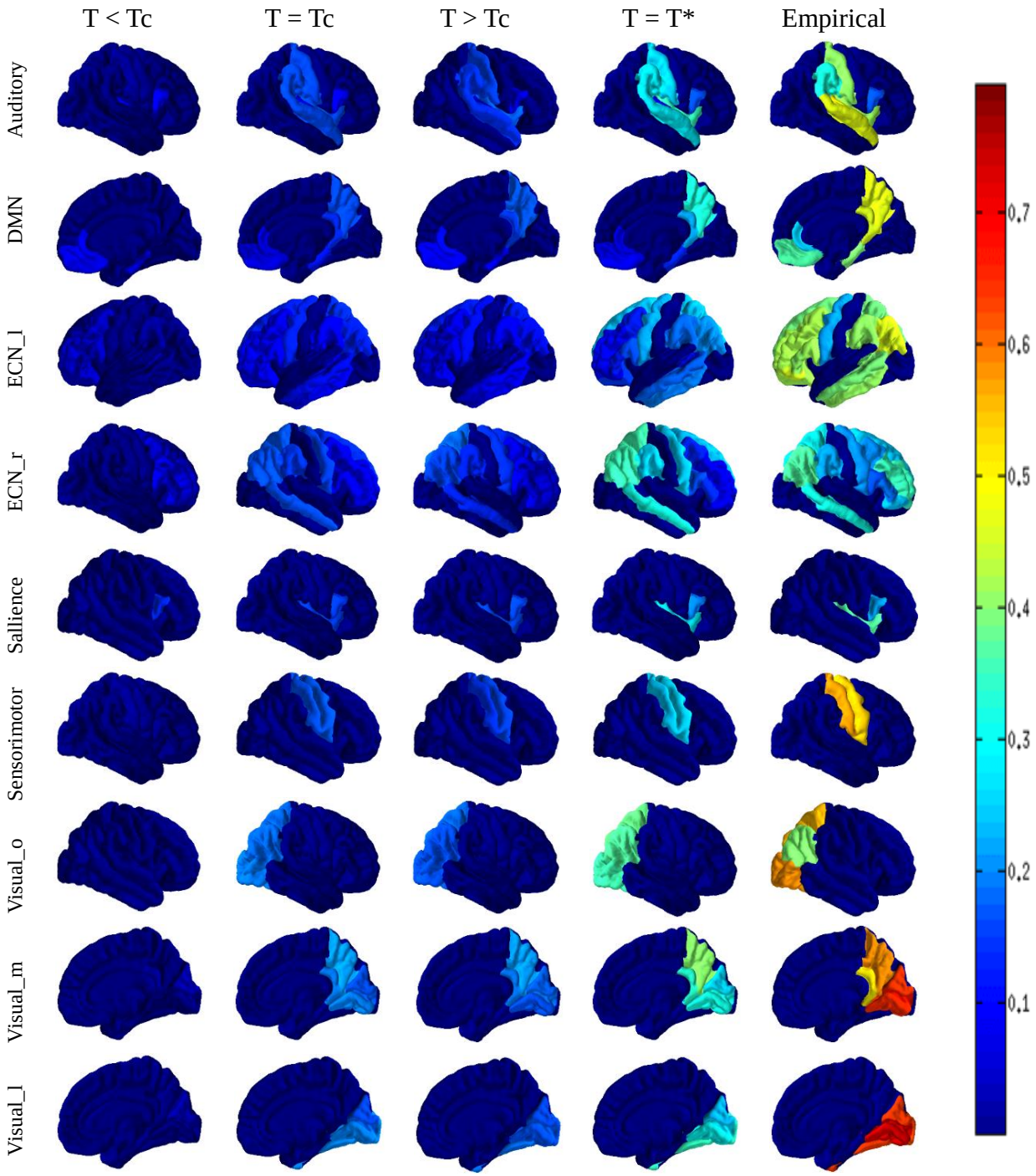

Figure 4.9: Brain maps of the resting state networks in generalized Ising model at four different temperatures, together with the empirical brain networks. Networks: DMN = Default Mode Network, ECN_l = External Control Network left, ECN_r = External Control Network right, Visua_o = Visual Occipital Network, Visual_m = Visual Medial Network, Visual_l = Visual Lateral Network.

Chapter 5

Discussion and Conclusions

The square lattice Ising model is one of the simplest models by which to show phase transition at the critical temperature. Using this simple model, it has been shown that a brain at rest could be simulated at the critical temperature of the model where the phase transition occurs [30]. This was justified by observing the behaviour of the model at the critical temperature which has a mixture of ordered and disordered states with long range correlations comparable with the brain's information integration and segregation. Thus we chose the two dimensional square lattice Ising model in our simulations. The simulations include two lattice sizes, 9×9 and 10×10 which were chosen because they result in 81 and 100 spin sites respectively, which then could be compared with the brain's 83 parcellations even though there is no one-to-one match. As expected, both of these configurations show the phase transition at the extracted critical temperature, which was validated with the prior results using the Equation 3.4 in Chapter 3.

We determined the critical temperature of the 2D classical Ising model from its magnetic susceptibility versus temperature graph as described in the methodology. The critical temperature value resulting from these plots agrees with the critical temperature described in [32] for the two lattice sizes 9×9 and 10×10. The behaviour of the energy and magnetization with temperature also agrees with previous results for the classical Ising model showing a phase

transition at the critical temperature.

Comparisons between the correlation in each model provide an overall insight into the data. As the classical Ising model is a more general model and does not have any spatial correspondence with the human brain, this model could be a good global measure by which to interpret the data. The nearest neighbour coupling is evident in the correlation maps of the classical Ising model shown in Figure 4.2. On the other hand, structural connectivity enhances the correlation patterns observed in the generalized Ising model in the same figure. As evident from the correlation maps, at $T < T_c$ the correlations are almost zero which is controversial to the fact that at low temperatures the spin configurations are ordered. If they are ordered, they should be highly correlated in terms of the spin time series due to the fact that they are highly unlikely to flip when tested for flip. Thus there will not be a variation of the spins as a function of time. When we use the Equation 3.1 to calculate the correlation of such two time series, the result will be undefined because of zero variance which is the denominator of the equation. To overcome this result, we added noise to the spin time series and when the correlation is calculated for such two noises it results in zero correlation, which explains the correlation maps for $T < T_c$. Furthermore, when the correlation maps of the generalized Ising model were analysed as a function of temperature, at T_c it did not provide a very good match with the empirical correlation. Thus, the distance between the correlation distributions were taken into account to find a temperature that minimizes the distance between the two cumulative distributions, and the results suggest that temperature is greater than T_c for the generalized Ising model. The analysis was continued by considering T_c as well as the new temperature T^*. The generalized Ising model gives a better match with the empirical correlation at T^* (Figure 4.4).

As expected, the distribution of the correlation in the classical Ising model shows a good match with the empirical data as it describes the global behaviour of the function. At T_c and T^* the models show some positive correlation that emphasizes the formation of clusters. From the

neurobiological perspective, neurons communicate with each other every second. The separate regions of the brain cannot work independently (even though they are structurally separated). Thus, they create clusters and networks to increase functional segregation, resulting in the positive correlation observed for the empirical data in Figure 4.5. On the other hand, the generalized Ising model does not show the expected behaviour at the critical temperature, which was determined from the susceptibility peak. However, it shows positive correlations as observed in empirical data at T^*.

We followed a data driven strategy to extract the graph theoretical networks from the correlation data. To do this, a threshold has to be selected such that it will allow accurate visualization of the networks. Thus, the thresholds play an important role in creating the networks using the correlations. From Figure 4.6, it is evident that the higher the threshold, the sparser the network will be as the average degree reduces as a power law while the threshold increases. Even though the classical Ising model acquires the maximum possible degree at the critical temperature, or at T^* with zero threshold, the generalized Ising model and the empirical network do not achieve such. This verifies the mixture of both positive and negative correlations observed for the fMRI data and generalized Ising model data in Figure 4.5. However, calculated global variables, such as the average degree and global efficiency, verify the match between the empirical data and the generalized Ising model at T^*, resulting in the highest functional integration measures.

Additionally, small-worldness plotted as a function of temperature in Figure 4.7 provides confirmation of the idea that the brain represents a small-world network with high clustering and low characteristic path lengths, representing high integration and segregation as described in [34, 35]. When the temperature reaches T_c for the classical Ising model and T^* for the generalized Ising model, both of the models converge to small-worldness as exhibited by the dynamical function of the brain. This small-world property depends on the clustering coeffi-

cient and the characteristic path length of the network being considered and a random network, as explained in Equation 2.10. The random network was created by preserving the degree distribution of the tested network to calculate the small-worldness. To explain the behaviour of the small-world property, clustering coefficients and the average path lengths are plotted as a function of temperature in Figure .2 in Appendix B. As the figure illustrates, even though the clustering coefficient is the highest at T_c or T^* for the models, the ratio of C/C_{rand} clearly shows a peak at a temperature less than T_c for the classical Ising model. However the ratio gives a minimum around T_c or T^*. On the other hand, when we consider the average path length, it clearly minimizes at T_c or T^* as expected. Nevertheless, due to a higher number of nodes governed by few connections, the average distance increases in the $T < T_c$ region. These facts result in the higher small-worldness for $T \neq T_c$ or T^* as seen in Figure 4.7.

The connectivity graphs of the generalized Ising model allow its visualization. When the graph at T_c and the graph of empirical data is compared, it is evident that the generalized Ising model does not exhibit similar behaviour with the empirical data as expected at the T_c (Figure 4.8). However, this implies that at T^* it creates more connections and the connectivity of the network is similar to that of the functional brain network. This result provides a platform for building the relationship between the structure and function of the brain, as the generalized Ising model was built based on structural connectivity (see the methodology).

Furthermore, studies of the resting state of the brain have provided information regarding possible functionally specialized resting state networks (RSNs). Figure 4.9 shows the brain maps of those nine resting state networks for the empirical data as well as for the simulated data, which shows a direct correspondence between the two types of data at T^*. Being able to extract these correlations with respect to the RSNs provide insight to the higher correlation lengths which allow the interactions between regions at a distance from each other, exhibited by the generalized Ising model. However, Figure 4.8 and 4.9 were created only for the gen-

eralized Ising model as it takes the 83 parcellations of the brain into account and the classical Ising model does not have any correspondence with the spatial parcellations of the brain.

Even though the Classical Ising model is able to explain the behaviour of the brain at the global level without any spatial specification, we need a better model to predict the connectivity of the structure and the function of the brain in a spatially accountable manner. As introduced in this research, the generalized Ising model better predicts the functional behaviour of the brain in relation to spatial positions of the brain than the classical Ising model. Additionally, the generalized Ising model, together with graph theory, is proven to facilitate the understanding of the relationship between the structure and the function of the brain. However, as discussed, the generalized Ising model provides the best fit for the empirical data at T^*, which is different from the critical temperature (T_c) which can be explained as below.

As observed in Figure 4.2, the classical Ising model resulted in positive correlations at T_c while the generalized Ising model had the majority of the correlations equal to zero at T_c. This was verified in Figure 4.5 with the mean of the distribution of correlation lying at zero for the generalized Ising model at T_c, while it was non-zero for the classical Ising model. However, at T^* the generalized Ising model was able to acquire the desired non-zero correlations similar to the empirical data (Figure 4.4), and the mean of the correlation distribution was shifted to 0.2 giving a better match with the empirical data which has a mean correlation of 0.3. Therefore, it could be sufficient to have only the critical temperature for the classical Ising model to obtain non-zero correlations as observed in the empirical data. However, to reproduce the behaviour of the empirical data the generalized Ising model should have an optimum temperature (T^*) as well as a given structural connectivity.

5.1 Future Directions

This research on the generalized Ising model was carried out together with graph theory only for healthy subjects. The results of this research demonstrate the possibility of applying this methodology to investigate the brain function of patients suffering from brain disorders due to severe brain injuries. The study would show the changes occurring in the functional activity of the brain through the changes in structural connectivity, which are extracted using DTI from patients. The comparison of the data between healthy subjects and patients would direct us to explore the connections necessary for rehabilitation of the injured brain. This could be very relevant in understanding the mechanism necessary to re-establish a normal structure-function relationship after injury and help in guiding the treatments for recovery of these patients.

Bibliography

[1] Sarah N. Koch. Brain Structure and Neurons. http://mybrainnotes.com/brain-cortex-neurons.html.

[2] Kristen Coyne. MRI: A Guided Tour. https://nationalmaglab.org/education/magnet-academy/learn-the-basics/stories/mri-a-guided-tour,2015.

[3] TK Das, PM Abeyasinghe, JS Crone, A Sosnowski, S Laureys, AM Owen, and A Soddu. Highlighting the structure-function relationship of the brain with the Ising model and graph theory. *BioMed research international*, 2014.

[4] KJ Friston, CD Frith, PF Liddle, and RSJ Frackowiak. Functional connectivity: the principal-component analysis of large (pet) data sets. *Journal of Cerebral Blood Flow and Metabolism*, 13:5, 1993.

[5] Andrew A Fingelkurts, Alexander A Fingelkurts, and Seppo Kähkönen. Functional connectivity in the brain: is it an elusive concept? *Neuroscience & Biobehavioral Reviews*, 28(8):827–836, 2005.

[6] Nikos K Logothetis. What we can do and what we cannot do with fMRI. *Nature*, 453(7197):869–878, 2008.

[7] Olaf Sporns, Giulio Tononi, and Rolf Kötter. The human connectome: a structural description of the human brain. *PLoS Computational Biology*, 1(4):e42, 2005.

[8] Florian Engert and Tobias Bonhoeffer. Dendritic spine changes associated with hippocampal long-term synaptic plasticity. *Nature*, 399(6731):66–70, 1999.

[9] Vernon B Mountcastle. *Perceptual neuroscience: The cerebral cortex*. Harvard University Press, 1998.

[10] Olaf Sporns, Giulio Tononi, and Gerald M Edelman. Connectivity and complexity: the relationship between neuroanatomy and brain dynamics. *Neural Networks*, 13(8):909–922, 2000.

[11] Steven Laureys, Philippe Peigneux, and Serge Goldman. Brain imaging. *Biological psychiatry*, pages 155–166, 2002.

[12] Peter Jezzard, Paul M Matthews, Stephen M Smith, et al. *Functional MRI: an introduction to methods*, volume 61.

[13] Seiji Ogawa, Tso-Ming Lee, Alan R Kay, and David W Tank. Brain magnetic resonance imaging with contrast dependent on blood oxygenation. *Proceedings of the National Academy of Sciences*, 87(24):9868–9872, 1990.

[14] David Attwell, Alastair M Buchan, Serge Charpak, Martin Lauritzen, Brian A MacVicar, and Eric A Newman. Glial and neuronal control of brain blood flow. *Nature*, 468(7321):232–243, 2010.

[15] Andrew Webb and George C Kagadis. *Introduction to biomedical imaging*. Wiley Hoboken, 2003.

[16] Peter J Basser, James Mattiello, and Denis LeBihan. MR diffusion tensor spectroscopy and imaging. *Biophysical journal*, 66(1):259, 1994.

[17] Heidi Johansen-Berg and Timothy EJ Behrens. *Diffusion MRI: from quantitative measurement to in vivo neuroanatomy*. Academic Press, 2013.

[18] Andrew L Alexander, Jee Eun Lee, Mariana Lazar, and Aaron S Field. Diffusion tensor imaging of the brain. *Neurotherapeutics*, 4(3):316–329, 2007.

[19] EO Stejskal and JE Tanner. Spin diffusion measurements: spin echoes in the presence of a time-dependent field gradient. *The journal of chemical physics*, 42(1):288–292, 1965.

[20] Kamal Shadi, Saideh Bakhshi, David A Gutman, Helen S Mayberg, and Constantine Dovrolis. A symmetry-based method to infer structural brain networks from tractography data. *arXiv preprint arXiv:1508.03788*, 2015.

[21] Yoshiki Kuramoto and Toshio Tsuzuki. On the formation of dissipative structures in reaction-diffusion systems reductive perturbation approach. *Progress of Theoretical Physics*, 54(3):687–699, 1975.

[22] Juan A Acebrón, Luis L Bonilla, Conrad J Pérez Vicente, Félix Ritort, and Renato Spigler. The Kuramoto model: A simple paradigm for synchronization phenomena. *Reviews of modern physics*, 77(1):137, 2005.

[23] Bryan C Daniels. Synchronization of globally coupled nonlinear oscillators: the rich behavior of the Kuramoto model. *Ohio Wesleyan Physics Dept., Essay*, 7(2), 2005.

[24] Steven H Strogatz. From Kuramoto to Crawford: exploring the onset of synchronization in populations of coupled oscillators. *Physica D: Nonlinear Phenomena*, 143(1):1–20, 2000.

[25] Michael VL Bennett and R Suzanne Zukin. Electrical coupling and neuronal synchronization in the mammalian brain. *Neuron*, 41(4):495–511, 2004.

[26] Joana Cabral, Henry Luckhoo, Mark Woolrich, Morten Joensson, Hamid Mohseni, Adam Baker, Morten L Kringelbach, and Gustavo Deco. Exploring mechanisms of spontaneous functional connectivity in meg: how delayed network interactions lead to structured amplitude envelopes of band-pass filtered oscillations. *Neuroimage*, 90:423–435, 2014.

[27] Stephen G Brush. History of the Lenz-Ising model. *Reviews of modern physics*, 39(4):883, 1967.

[28] Dante R Chialvo. Emergent complex neural dynamics. *Nature physics*, 6(10):744–750, 2010.

[29] David P Landau and Kurt Binder. *A guide to Monte Carlo simulations in statistical physics*. Cambridge University Press, 2014.

[30] Daniel Fraiman, Pablo Balenzuela, Jennifer Foss, and Dante R Chialvo. Ising-like dynamics in large-scale functional brain networks. *Physical Review E*, 79(6):061922, 2009.

[31] Daniele Marinazzo, Mario Pellicoro, Guorong Wu, Leonardo Angelini, Jesús M Cortés, and Sebastiano Stramaglia. Information transfer and criticality in the Ising model on the human connectome. *PloS one*, 9(4):e93616, 2014.

[32] Lilian Witthauer and Manuel Dieterle. The phase transition of the 2d-Ising model, 2007.

[33] Joana Cabral, Etienne Hugues, Olaf Sporns, and Gustavo Deco. Role of local network oscillations in resting-state functional connectivity. *Neuroimage*, 57(1):130–139, 2011.

[34] Ed Bullmore and Olaf Sporns. Complex brain networks: graph theoretical analysis of structural and functional systems. *Nature Reviews Neuroscience*, 10(3):186–198, 2009.

[35] Mikail Rubinov and Olaf Sporns. Complex network measures of brain connectivity: uses and interpretations. *Neuroimage*, 52(3):1059–1069, 2010.

[36] Vito Latora and Massimo Marchiori. Efficient behavior of small-world networks. *Physical review letters*, 87(19):198701, 2001.

[37] Olaf Sporns, Dante R Chialvo, Marcus Kaiser, and Claus C Hilgetag. Organization, development and function of complex brain networks. *Trends in cognitive sciences*, 8(9):418–425, 2004.

[38] Raymond Salvador, John Suckling, Martin R Coleman, John D Pickard, David Menon, and ED Bullmore. Neurophysiological architecture of functional magnetic resonance images of human brain. *Cerebral cortex*, 15(9):1332–1342, 2005.

[39] Rahul S Desikan, Florent Ségonne, Bruce Fischl, Brian T Quinn, Bradford C Dickerson, Deborah Blacker, Randy L Buckner, Anders M Dale, R Paul Maguire, Bradley T Hyman, et al. An automated labeling system for subdividing the human cerebral cortex on mri scans into gyral based regions of interest. *Neuroimage*, 31(3):968–980, 2006.

[40] Stephan Gerhard, Alessandro Daducci, Alia Lemkaddem, Reto Meuli, Jean-Philippe Thiran, and Patric Hagmann. The connectome viewer toolkit: an open source framework to manage, analyze, and visualize connectomes. *Frontiers in neuroinformatics*, 5, 2011.

[41] Leila Cammoun, Xavier Gigandet, Djalel Meskaldji, Jean Philippe Thiran, Olaf Sporns, Kim Q Do, Philippe Maeder, Reto Meuli, and Patric Hagmann. Mapping the human connectome at multiple scales with diffusion spectrum MRI. *Journal of neuroscience methods*, 203(2):386–397, 2012.

[42] Alessandro Daducci, Stephan Gerhard, Alessandra Griffa, Alia Lemkaddem, Leila Cammoun, Xavier Gigandet, Reto Meuli, Patric Hagmann, and Jean-Philippe Thiran. The connectome mapper: an open-source processing pipeline to map connectomes with MRI. *PloS one*, 7(12):e48121, 2012.

[43] TEJ Behrens, H Johansen Berg, Saad Jbabdi, MFS Rushworth, and MW Woolrich. Probabilistic diffusion tractography with multiple fibre orientations: What can we gain? *Neuroimage*, 34(1):144–155, 2007.

[44] Aapo Hyvärinen, Juha Karhunen, and Erkki Oja. *Independent component analysis*, volume 46. John Wiley & Sons, 2004.

[45] Wei Cai. Ising Model. `http://micro.stanford.edu/~caiwei/me334/Chap12_Ising_Model_v04.pdf,2011`.

Appendices

.1 Appendix A: MATLAB code for simulations of the generalized Ising model

(The code was modified from a previous version written by Dr. T. K. Das)

```
%==========================================================================
%
% Monte Carlo Methods for the evaluation of the thermodynamic
% properties of the generalized Ising model with coupling defined
% by the connectivity matrix obtained from DTI
% ==========================================================================


clear all;

load MJ_all.mat;

MJ = MJ_all_mn(:,:);
J = MJ./max(max(MJ)); % Normalizing the coupling

N = 83; % Dimension of the connectivity matrix

% Selection of the range of temperature for the model
temp = 0.5:0.01:3.01;

[m1, m2]=size(J);
time_corr=198; % Predefining the number of time points needed

% Predefining the number of flips needed to equillibrate
t_eq=m1*m2*100;

no_flip = t_eq; % No of flip at each temperature

% Obtaining the equillibrium configuration no_bin times
no_bin = 5;

% A coordinate matrix is generated from random permutation of N
randcoord = randperm(N);

count = 0;
temp_len = length(temp);
Ener = zeros(1,temp_len);
```

```
Mag = zeros(1, temp_len);
Spec_Heat= zeros(1, temp_len);
Sus = zeros(1, temp_len);
Corr_DTI = zeros(N,N, temp_len);
S = zeros(N,time_corr,temp_len);

for T = temp;

    % Initial spin configuration
    spin_vec = (rand(N,1) > 0.5)*2 - 1;

    count = count + 1;
    mag = sum(spin_vec);
    for b = 1 :no_bin;
        ener_sum = 0;
        ener_sqr_sum = 0;
        mag_sum = 0;
        mag_sqr_sum = 0;
        nn = 0;
        for i = 1:no_flip;
  % Run through the N points of the coordinate matrix once, and
  % when the counter is larger than N, it goes back to the first
  % point, and the coordinate is rerandomized before it is called
  % upon. This ensures the random but unique choice of index when
  % checking to flip.
            nn = nn + 1;
            if (nn > N);
                nn = nn-N;
                randcoord = randperm(N);
            end
            Flip = randcoord(nn);
            % Compute the change in energy
            dE=0;
            for j=1:N
                if (j~= Flip)
                    dE = dE + J(Flip,j)*spin_vec(j);
                end
            end
            dE=2*dE*spin_vec(Flip);

            % Desiding whether to accept or reject the flip
            if (dE <= 0);
                spin_vec(Flip) = - spin_vec(Flip);
                mag = mag + 2*spin_vec(Flip);
            elseif (rand <= exp(-dE/T));
```

```
            spin_vec(Flip) = - spin_vec(Flip);
            mag = mag + 2*spin_vec(Flip);
        end
        ener = 0;
        for ii = 1:N;
            for jj=ii+1:N
            ener = ener - J(ii,jj)*spin_vec(ii)*spin_vec(jj);
            end
        end
        ener_sum = ener_sum + ener;
        mag_sum = mag_sum + mag;
        ener_sqr_sum = ener_sqr_sum + ener^2;
        mag_sqr_sum = mag_sqr_sum + mag^2;
    end
    ener_mean(b) = ener_sum/no_flip;
    mag_mean(b) = mag_sum/no_flip;
    ener_sqr_mean(b) = ener_sqr_sum/no_flip;
    mag_sqr_mean(b) = mag_sqr_sum/no_flip;
    specheat_mean(b) = (ener_sqr_mean(b)-(ener_mean(b))^2)/N/T^2;
    sus_mean(b) = (mag_sqr_mean(b)-(mag_mean(b))^2)/N/T;
end
Ener(count) = mean(ener_mean)/N ;
Mag(count) = mean(mag_mean)/N ;
Spec_Heat(count)= mean(specheat_mean)/N ;
Sus(count)= mean(sus_mean)/N ;

% Generating 198 time points for each of the spinsites

mm = 0;
for jj = 1:time_corr;
    for i = 1:N;
        % Compute the change in energy
        mm = mm + 1;
        if (mm > N);
            mm = mm-N;
            randcoord = randperm(N);
        end
        Flip = randcoord(mm);
        dE = 0;
        for j=1:N
            if (j~=Flip)
                dE = dE + J(Flip,j)*spin_vec(j);
            end
        end
        dE=2*dE*spin_vec(Flip);
```

```
            % Desiding whether to accept or reject the flip
            if (dE <= 0);
                spin_vec(Flip) = - spin_vec(Flip);
            elseif (rand <= exp(-dE/T));
                spin_vec(Flip) = - spin_vec(Flip);
            end
        end

        % timepoints x spinsites x temperature
        S(:,jj,count)=spin_vec;
    end

    % Correlation matrix
    Corr_DTI(:,:, count)=corrcoef(squeeze(S(:,:, count))');
    Sus(count)= mean(sus_mean)/N ;
    display([num2str(count)])

end
```

.2 Appendix B: Supplementary figures

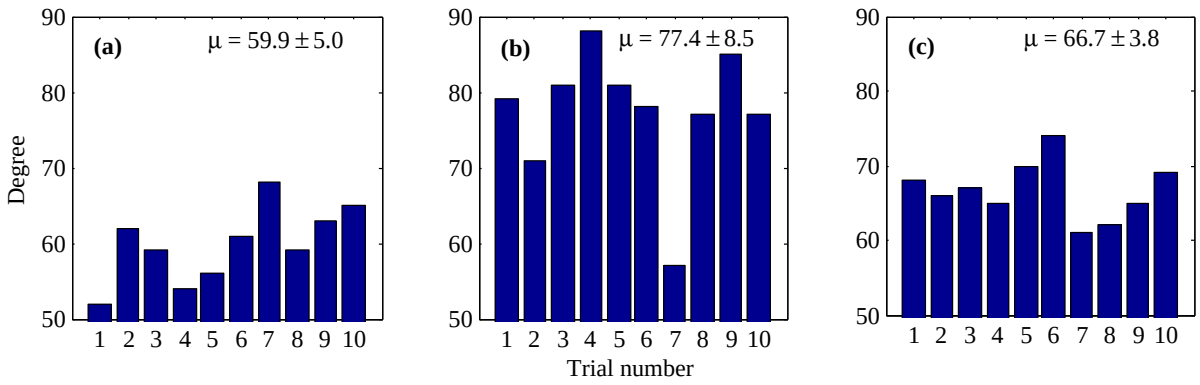

Figure .1: Variation of the degree in node 20 for different simulations of the Classical Ising model (a). 9×9 ,(b). 10×10 and (c). the Generalized Ising model. μ represents the mean degree over realizations for the same node.

Figure .1 was plotted to observe the variations in local degree (degree of a single node) as we repeat the simulations ten times starting with a different initial spin configurations always. It shows a higher variance in the mean degree of the selected node for the classical Ising model than the generalized Ising model. The low variance observed in the generalized Ising model can be explained from the well defined structural connectivity used in the simulations of the model which was extracted from DTI.

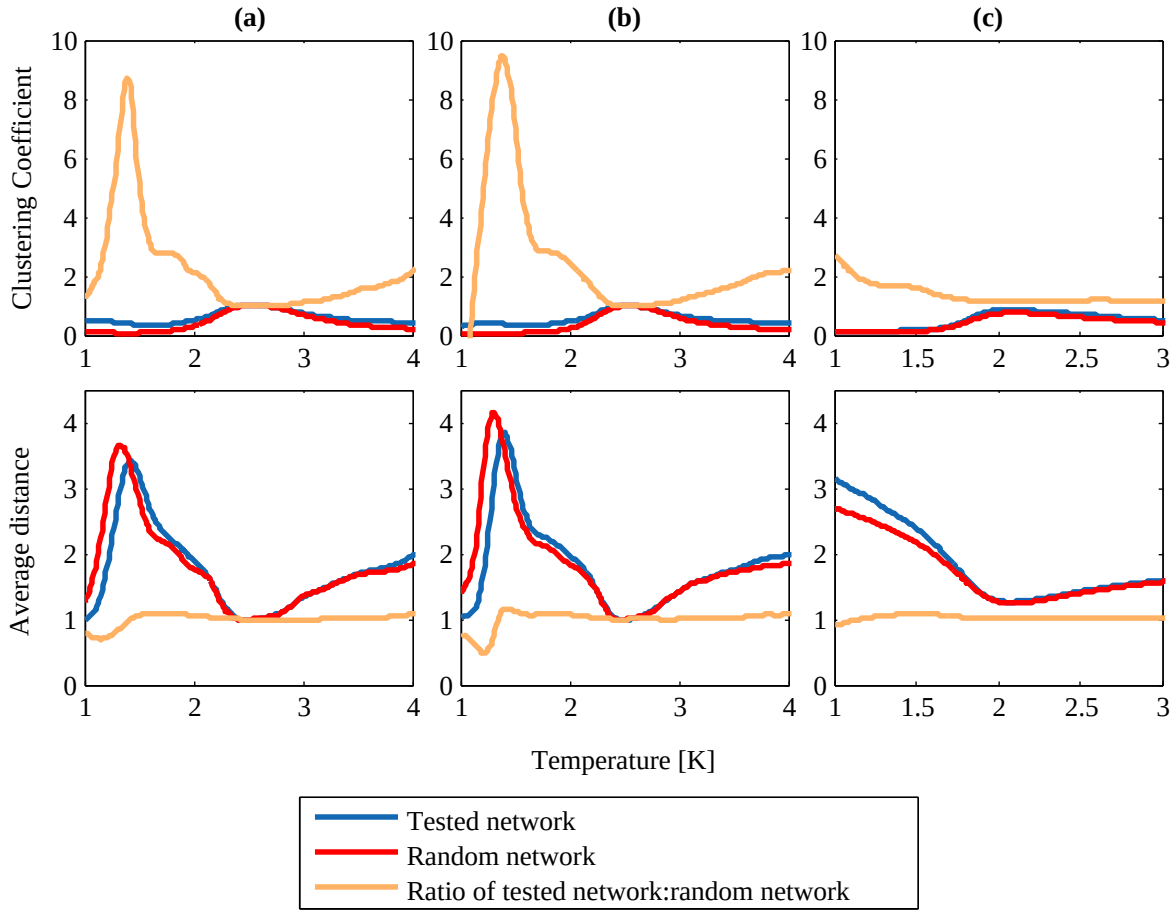

Figure .2: Clustering coefficient (C) and the average path length (L) of the tested network and a random network with the ratio for C/C_{rand} and L/L_{rand} respectively as a function of temperature for the Classical Ising model (a) 9×9 ,(b) 10×10 and (c) the generalized Ising model.

Figure .2 was plotted to explain the behaviour of the small-worldness as a function of temperature in the models. Following equation was used to calculate the clustering coefficient:

$$C = \frac{1}{n}\sum_{i \epsilon N} C_i = \frac{1}{n}\sum_{i \epsilon N} \frac{2t_i}{k_i(k_i - 1)} \tag{1}$$

where C_i is the clustering coefficient of the i^{th} node, k_i is the degree of node i, n is the number of nodes in the network and t_i is the number of triangles around node i. Average distance for

the netwrok can be calculated using Equation 2:

$$L = \frac{1}{n}\sum_{i \epsilon N} L_i = \frac{1}{n}\sum_{i \epsilon N} \frac{\sum_{j \epsilon N,\, j \neq i} d_{ij}}{n-1} \tag{2}$$

where L_i is the average distance of the i^{th} node, n is the number of nodes in the network and d_{ij} is the shortest path length between the i^{th} and the j^{th} nodes.

.3 Appendix C: Labels of 83 Parcellations of the Brain

Right hemisphere

1. lateral-orbito-frontal
2. pars-orbitalis
3. frontal-pole
4. medial-orbito-frontal
5. pars-triangularis
6. pars-opercularis
7. rostral-middle-frontal
8. superior-frontal
9. caudal-middle-frontal
10. pre-central
11. para-central
12. rostral-anterior-cingulate
13. caudal-anterior-cingulate
14. posterior-cingulate
15. isthmus-cingulate
16. post-central
17. supra-marginal
18. superior-parietal
19. inferior-parietal
20. precuneus
21. cuneus
22. pericalcarine
23. lateral-occipital
24. lingual
25. fusiform
26. para-hippocampal
27. entorhinal
28. temporal-pole
29. inferior-temporal
30. middle-temporal
31. bankssts
32. superior-temporal
33. transverse-temporal
34. insula
35. thalamus-proper
36. caudate
37. putamen
38. pallidum
39. accumbens-area
40. hippocampus
41. amygdala

Left hemisphere

42. lateral-orbito-frontal
43. pars-orbitalis
44. frontal-pole
45. medial-orbito-frontal
46. pars-triangularis
47. pars-opercularis
48. rostral-middle-frontal
49. superior-frontal
50. caudal-middle-frontal
51. pre-central
52. para-central
53. rostral-anterior-cingulate
54. caudal-anterior-cingulate
55. posterior-cingulate
56. isthmus-cingulate
57. post-central
58. supra-marginal
59. superior-parietal
60. inferior-parietal
61. precuneus
62. cuneus
63. pericalcarine
64. lateral-occipital
65. lingual
66. fusiform
67. para-hippocampal
68. entorhinal
69. temporal-pole
70. inferior-temporal
71. middle-temporal
72. bankssts
73. superior-temporal
74. transverse-temporal
75. insula
76. thalamus-proper
77. caudate
78. putamen
79. pallidum
80. accumbens-area
81. hippocampus
82. amygdala

83. brainstem (does not belong to the right or the left hemisphere)

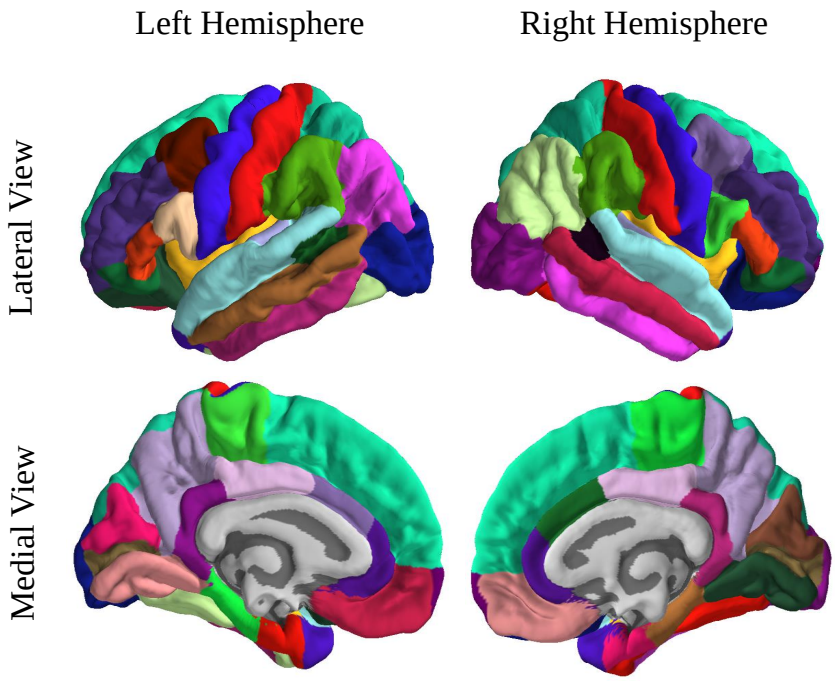

Figure .3: Brain maps for four different views of the 83 parcellations in the brain.

.4 Appendix D: Representation of the Resting State Networks

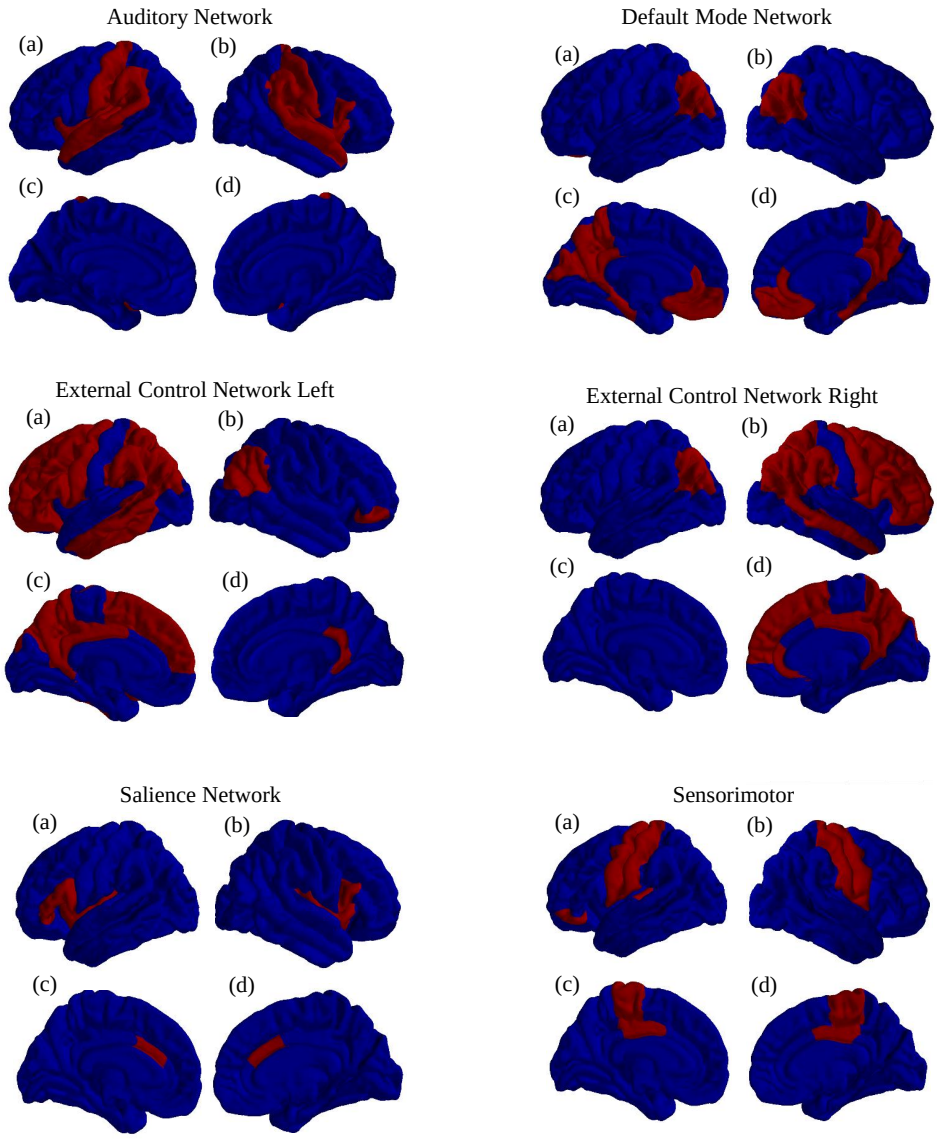

Figure .4: Representation of the resting state networks in the brain: (a) lateral view of the left hemisphere, (b) lateral view of the right hemisphere, (c) medial view of the left hemisphere and (d) medial view of the right hemisphere. Red indicates the regions belong to the network and blue indicates the regions which does not belong to the network.

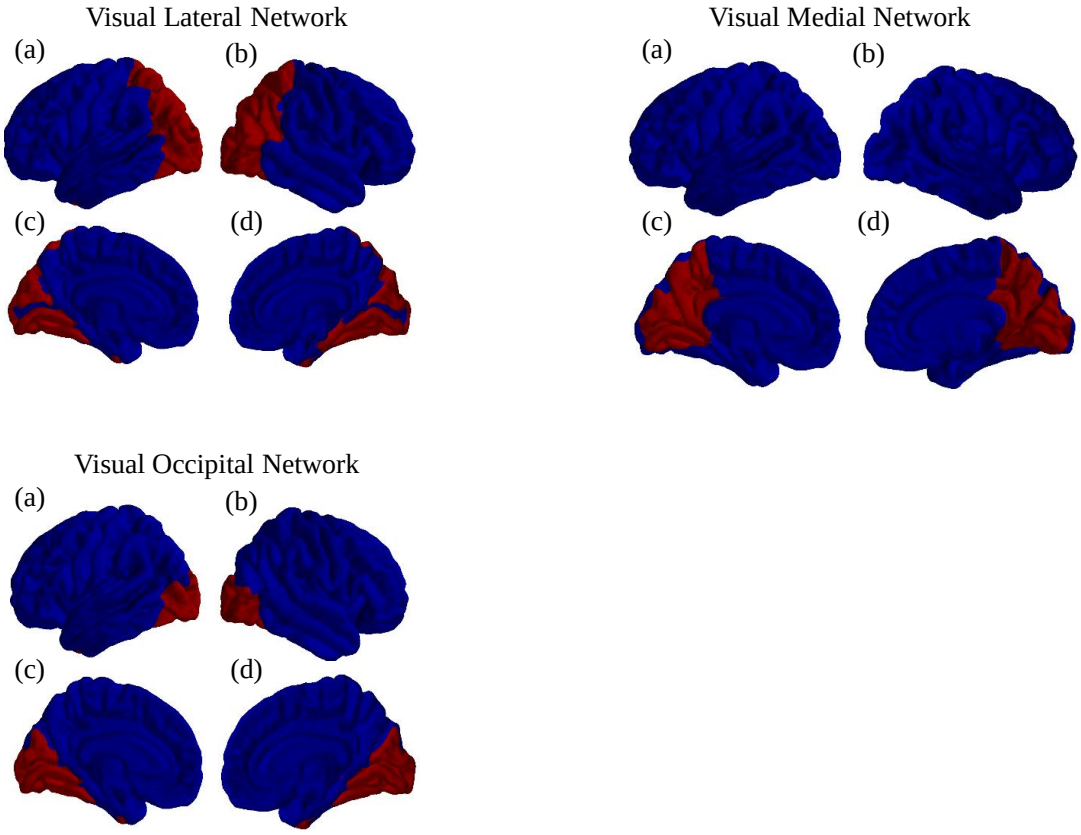

Figure .5: Representation of the resting state networks in the brain: (a) lateral view of the left hemisphere, (b) lateral view of the right hemisphere, (c) medial view of the left hemisphere and (d) medial view of the right hemisphere. Red indicates the regions belong to the network and blue indicates the regions which does not belong to the network.

Curriculum Vitae

Name:	Pubuditha Abeyasinghe
Post-Secondary Education and Degrees:	University of Sri Jayewardenapura, Sri Lanka B.Sc. degree in Physics (First Class) 2008-2012
Honours and Awards:	Western Graduate Research Scholarship, 2013 - 2015 Western Teaching and Research Assistantship, 2013 - 2015
Related Work Experience:	Teaching Assistant Department of Physics and Astronomy The University of Western Ontario 2013 - 2015 Teaching Assistant Department of Physics University of Sri Jayewardenapura 2013
Publications:	TK Das, PM Abeyasinghe, JS Crone, A Sosnowski, S Laureys, AM Owen, and A Soddu. **Highlighting the Structure- Functional Relationship of the Brain with the Ising Model and Graph Theory**. *BioMed research international*, 2014;2014:237898. doi: 10.1155/2014/237898. Epub 2014 Sep 4. Contribution: Composed the section about graph theory and generated the relevant figures in that section. PM Abeyasinghe, TK Das, DR Paula, AM Owen and A Soddu. **Structure - Function Relationship of the Brain: Introducing the Generalized Ising Model** (in preparation).

DR Paula, E Ziegler, PM Abeyasinghe, C Cavalier, L Heine, C di Perri, A Demertzi, Q Norhomme, VC Verville, A Vanhaudenhuyse, J Stender, F Gomez, L Tshibanda, s Laureys, AM Owen, TK Das, and A Soddu. **A method for within-component graph analysis of resting-state fMRI** (in preparation).
Contribution: Helped with the graph theoretical analysis.

Conference Presentations:

PM Abeyasinghe, TK Das, DR Paula, AM Owen and A Soddu. **Modeling the Relationship between the Anatomical Structure and the Functional Connectivity of the Brain.** Poster session to be presented at: Engineering the Brain: Technologies for Neurobiological Applications, 2015 October 15-16, Chicago, IL. (Abstract was accepted for the poster session).

PM Abeyasinghe, DR Paula, S Laureys, AM Owen, TK Das and A Soddu. **Modeling the Relationship between the Anatomical Structure and the Functional Connectivity of the Brain.** Poster session presented at: The interdisciplinary research showcase, 2014 December 2, The Western University, London, ON.

TK Das, PM Abeyasinghe, A Sosnowski, S Khajehabdollahi, B Ge, S Laureys, AM Owen and A Soddu. **Modeling Functional Organizations of the Resting Brain using the Anatomical Structure**. Poster session presented at: 34th Annual meeting of the Southern Ontario Neuroscience Association, 2014 May 5, The Western University, London, ON.